SRON
Netherlands Institute for Space Research

university of groningen

Modelling kinetic inductance detectors and associated noise sources

INDUSTRIAL INTERNSHIP PROJECT REPORT

29 JULY 2020

Author:
Kaushal Marthi
S3318206

Supervisor:
Dr. Stephen Yates
SRON Groningen

Summary

In order to improve the performance of ground-based astronomical instrumentation, it is key to be able to predict the expected noise sources during detection, in order to design noise mitigation strategies.

The effect of the sky and atmosphere fluctuations is generally the main challenge for ground-based instrumentation, and to that end a simulator for the instrument DESHIMA (Deep Spectroscopic High-redshift Mapper) has been developed, known as TiEMPO (Time-dependent End-to-end Model for Post-process Optimization) [1] [2]. This uses an atmospheric model known as ARIS, which simulates the noise and transmission of the sky [3].

This project was designed to address the next step in the replication of noise sources: the sources related to the detector, and the signal which is read out. The detectors in question are kinetic inductance detectors (KIDs), which measure a signal by a change in phase of a superconducting resonant circuit caused by photon absorption modifying the kinetic inductance.

The KID model was hence designed, and coded in Python 3, to convert temperature to KID phase, whilst adding noise sources. This used a model by Takekoshi et al. [4], for the normalised frequency shift caused by absorbed radiation from a load of a given effective temperature.

Data for DESHIMA 1.0 was available, hence the desire was to replicate a DESHIMA 1.0 observation, by combining a simulation from TiEMPO with the KID model, and analyse the output. The TiEMPO simulation was an iterative process, with certain settings changed in order to obtain greater similarity to observed data. Justifications are provided for the changes made.

Initial simplified analysis of the output of the TiEMPO (before passing through KID model) showed, when the off-source data is subtracted from the on-source, that an emission

line at 350 GHz can be observed, but that there is too much residual from the sky to easily observe continuum emission.

The sky temperature data was subsequently passed through the KID model, to give a noisy signal in KID phase. The analysis of the noise at output was performed through the use of power spectra and integration of the noise. The power spectra were analysed for their similarity to the spectra from the data of the DESHIMA 1.0 observation, and the noise integration, performed on simulated data only, was in order to observe if the noise would decrease with integration time.

Statistical analysis of the differences in noise levels between the simulated and observed data showed a fair amount of scatter across the KIDs, and seemed to show a small systematic offset in the peak. A likely erroneous repeat usage of the forward efficiency can partially account for this offset.

Often a large difference in phase values between simulation and observation was noticed, with a large scatter across KIDs was also observed. These features are likely due to limitations in the model, and a lack of precise knowledge of the KID calibration and operation.

The noise integration, performed using Allan variance, showed an expected pattern of reduction in noise until a certain point in time (Allan time), after which it increases once more. The decline corresponds to the white noise part of the spectrum, and the subsequent incline is when the 1/f noise dominates. The Allan time showed a value of around 0.5s. This is expected, as this corresponds roughly to the frequency value in the spectrum where the 1/f noise begins to dominate.

The aim of the project was to formulate a KID model, and use it in the replication of an observation by DESHIMA 1.0. The aim can be considered to be achieved to a reasonable extent, given that the model was formulated and was used in the creation of reasonably well matching spectra. Certain unexpected results however, do indicate limitations in the model, particularly

with the values of the phase offsets between measurement and simulation. These limitations are likely to do with the simplifications in the model. These include the assumptions of KID symmetry, and recent calibration of the KIDs. The lack of knowledge of the operation of the KIDs is reflected by the unexpected positive values observed in the measured phase data, indicating a sky temperature higher than 300K, which should not be possible. The usage of a singular parameter for the optical efficiency is another limitation, especially at the edges of the band, where the values had increased variation.

Contents

1 Introduction

1.1 Background

There are many questions about the nature and characteristics of the universe that remain open, and many other areas about which more knowledge is desired. The asymmetry between matter and antimatter, the dark energy issue, the formation of galaxies to name but three. In this regard the early universe has potential to provide key insights, thus there is a constant drive to probe deeper into the early universe, and analyse the observations at high redshifts.

The relentless need to probe deeper to the early universe leads to continually increasing requirements on astronomical instrumentation, especially when it comes to reducing and/or eliminating the effects of noise sources. Ground-based instrumentation in particular, has additional challenges in this field, namely the noise produced by atmospheric fluctuations. These tend to produce a large amount of noise, which leads to an obscured signal and diminished signal-to-noise ratio (SNR). This requires not only high-quality detectors, but well-designed noise mitigation strategies to overcome. These can be best designed when there is clear knowledge of, and ability to reproduce, noise sources existing in the path between emission and measurement at the readout.

1.2 Simulation of noise sources

The instrument under consideration in this project is known as the Deep Spectroscopic High-redshift Mapper (DESHIMA), which is an instrument in place on the Atacama Submillimeter Telescope Experiment (ASTE). It is a far-infrared camera, which aims to "gain a better understanding of how stars are formed in star systems enclosed by matter" [1]. The initial version of DESHIMA (1.0), uses 49 spectral channels, and performed observations in 2017 [1]. An upgraded version, known as DESHIMA 2.0, is being planned for the future, with 347 spectral channels planned over a significantly wider band than DESHIMA 1. This

instrument should provide a significant improvement upon the efficiency and sensitivity of DESHIMA 1.0.

In order to reproduce the noise existing from the atmospheric fluctuations, and how this is transmitted through DESHIMA, TiEMPO (Time-dependent End-to-end Model for Post-process Optimization) was formulated by Esmee Huijten [2]. This makes use of a model which simulates the atmospheric fluctuations which lead to changes in atmospheric transmission and cause noise, known as ARIS [3]. In combination with ARIS, TiEMPO simulates the transmission of the signal from the sky through the components of DESHIMA using radiative transfer up to the detector. The power reaching the detector is then converted back to sky temperature, making this effectively the sky temperature that is 'seen' by the detector.

With the development of a model to accurately simulate the signal being received at the detector due to the atmosphere, noise mitigation strategies can be designed based on simulated data, before use on the real instrument. For example, strategies for chopping can be implemented in the simulation in order to judge their success in reducing noise, and so in turn being able to observe weak astronomical features that would previously have been lost in noise.

The simulator for DESHIMA reaches to the point of absorption at the detector, but does not model the detector. The next step would be modelling the noise sources after this point. This report, therefore, will address the formation of a model which attempts to reproduce the noise sources which exist when a signal is measured by Kinetic Inductance Detectors (KIDs) [5], which are the detectors used in DESHIMA. These include the noise sources of the KIDs, and the electronics by which the signal is read out.

1.3 Aims & Objectives

The overall aim of the project would be to formulate a KID model including noise sources, observe the total simulated noise, and analyse its characteristics, particularly with regards to integration over time. The desired outcome is that the simulated noise integrates

down with longer observation time, and that the SNR therefore increases, as seen in **Figure 1.1** [6]. This overall aim is then broken down into sequential objectives which are summarised below:

1. **KID model development –** A model which would take the output signal from the sky simulator, and convert to the signal output from a KID, whilst also adding the relevant noise sources.
2. **Replication of observed data –** Combining the sky simulator and KID model, and attempt to replicate the data measured by DESHIMA
3. **Analysis of noise at output –** Observing spectra to analyse frequency dependence, carrying out noise integration.

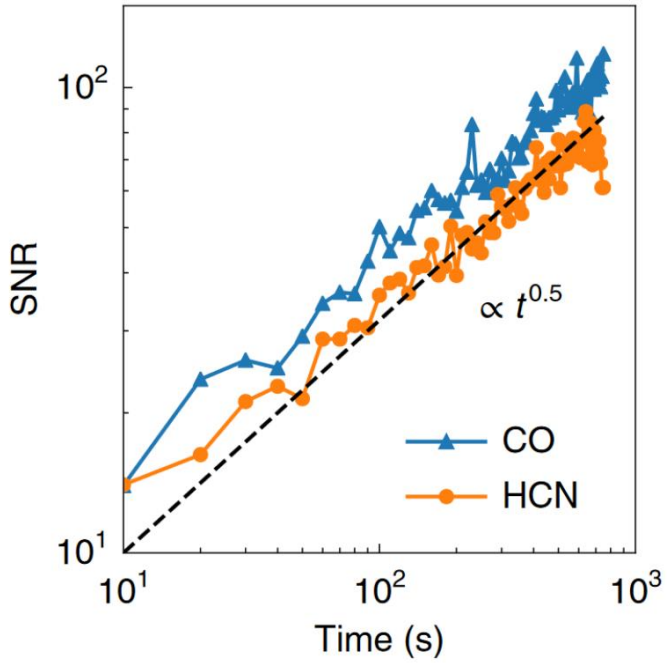

Figure 1.1: Figure from DESHIMA Nature paper, showing the increase of SNR over integration time [6]

2 Theoretical Background

In order to describe the development of the model of the KIDs and the noise sources, it is useful to explain the theory of KIDs and describe the noise sources associated with the detection of a signal by a KID.

2.1 Kinetic Inductance Detectors (KIDs)

2.1.1 Theory of KIDs

In a superconducting material below the critical temperature, the impedance is dependent on the kinetic inductance, which in turn is caused by the inertia of the Cooper pairs. Cooper pairs do not have resistance, hence the superconductivity [7]. However, the particles that exist singularly, known as quasiparticles, do have resistance, and a different inductance. Incoming radiation breaks Cooper pairs and creates quasiparticles, as seen in **Figure 2.1** [7]. This in turn causes a change in the resistance and inductance, therefore a change in the real and imaginary parts of the overall impedance.

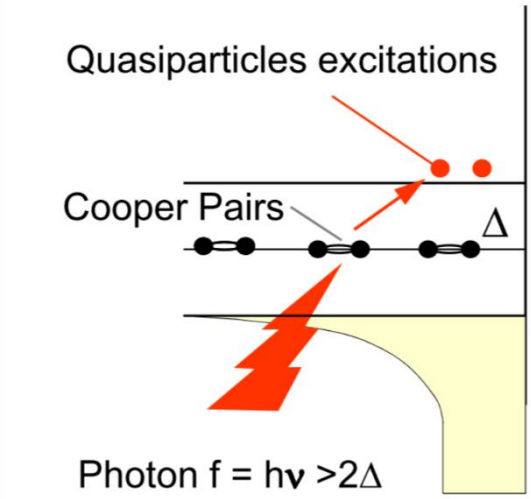

Figure 2.1: Illustration of incoming radiation breaking Cooper pairs, and creating quasiparticles [7]

KIDs are constructed by making a superconducting material part of a resonant circuit. Therefore, this change in impedance results in a change in resonant frequency and phase of the resonant circuit, as can be seen in **Figure 2.2** [7].

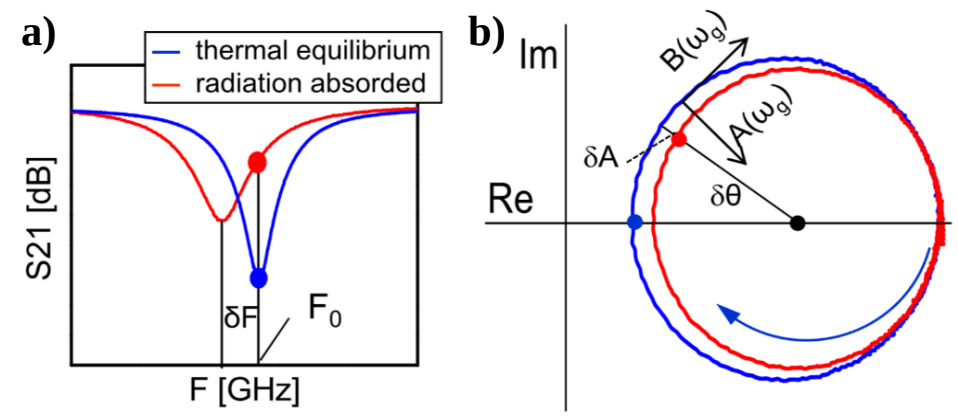

Figure 2.2: Figure showing the **a)** complex transmission S_{21} of KID, for a sweep of the frequencies around resonance, along with **b)** the corresponding circle of the phase [7].

2.1.2 Model of KIDs

In the complex plane, the resonant circuit of a KID (z) can be described by **Equation (2.1)** (KID equations: private communication S. Yates, derived from B. Mazin PhD thesis [8]). This is offset relative to the centre of the KID circle.

$$z = \frac{S + X^2}{1 + X^2} - \left(\frac{1 + S}{2}\right) + i\frac{X(1 - S)}{1 + X^2}$$

(2.1)

The parameter X describes the frequency shift from resonance, and is normalised by the resonant frequency and half bandwidth:

$$X = 2Q_L\delta x$$

(2.2)

Q_L is the loaded Q factor, and δx is the normalised frequency shift from the resonant frequency (f_0). These are given by **Equation (2.3)**, where Q_i and Q_c are the internal and coupling Q factors, respectively. These describe the losses in the system and the coupling to the feedline, respectively [7].

$$\delta x = \frac{f - f_0}{f_0}, \qquad Q_L = \frac{Q_i Q_c}{Q_i + Q_c}$$

(2.3)

The parameter S is the dip depth (or minimum dip transmission), as can be seen in **Figure 2.2** a), and is given by [8]:

$$S = S_{21}^{min} = \frac{Q_c}{Q_i + Q_c} \tag{2.4}$$

The term $-\left(\frac{1+S}{2}\right)$ in **Equation (2.1)** represents the offset of the KID circle to zero. The offset of the edge of the KID circle from zero is S, and the radius of the KID circle is given by $\frac{1-S}{2}$, as can be seen in **Figure 2.3** below. Hence, the KID circle centre is offset to zero by subtracting $\frac{1+S}{2}$.

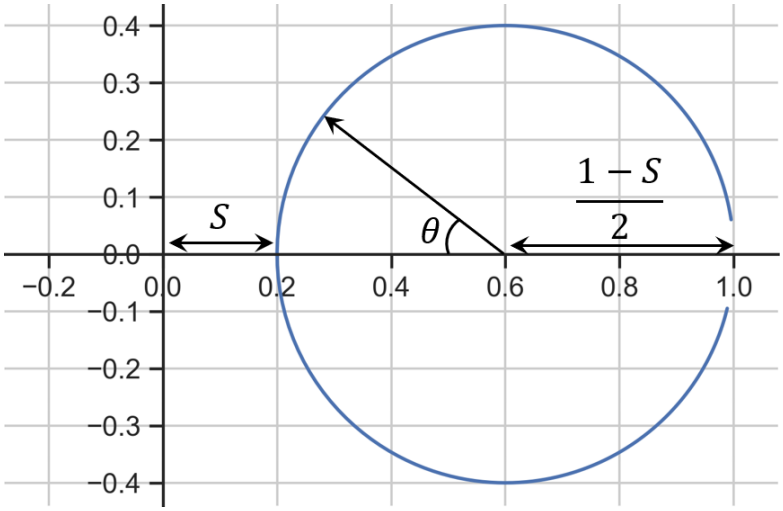

Figure 2.3: Illustration of KID circle, from a temperature sweep. Figure shows offset and radius of KID circle

The relation between the normalised frequency shift X and the phase of the resonant circuit θ is given by:

$$\theta = 2 \arctan X \tag{2.5}$$

2.2 Noise Sources

Various effects in the path between the atmosphere and the measurement of a signal at the read-out lead to a noise source. These noise sources and their causes are described in this section. The incoming signal and hence the noise sources can be converted to various domains,

which is key because certain sources will be created in different domains, due to their causes. These signal domains include the KID phase as in **Equation (2.5)**, the normalised frequency shift off-resonance of the resonant circuit δx (also called KID frequency), the effective sky temperature, and the carrier signal which carries the information. The levels of noise sources would change depending on which domain they are in.

2.2.1 Noise sources incident on detector

There are two primary noise sources associated with the photons incident upon a detector: the sky fluctuations and the photon noise. The sky fluctuations are associated with the fluctuations of the atmosphere, leading to fluctuations in the atmospheric transmission which in turn affects the arrival rates of the photons and varies the amount of loading from the atmosphere. Unstable, drifting systems produce a noise spectrum with a shape of $1/f^n$ due to the sky fluctuations, where f represents the frequencies of the signal.

The photon noise, on the other hand, is related to the Poisson noise in the arrival rate of photons, and the tendency of photons to group (photon bunching) [9]. Since photons will not consistently arrive at a rate of x photons/second at a detector, there is some noise in the amount of power measured by the detector. The photon noise is white, i.e. has no frequency dependence, and is therefore flat in the power spectrum. **Figure 2.4** below illustrates the combination of these two noise sources, showing that at low frequencies the sky noise ($1/f^n$) dominates, whereas at higher frequencies, the sky noise drops into the photon noise.

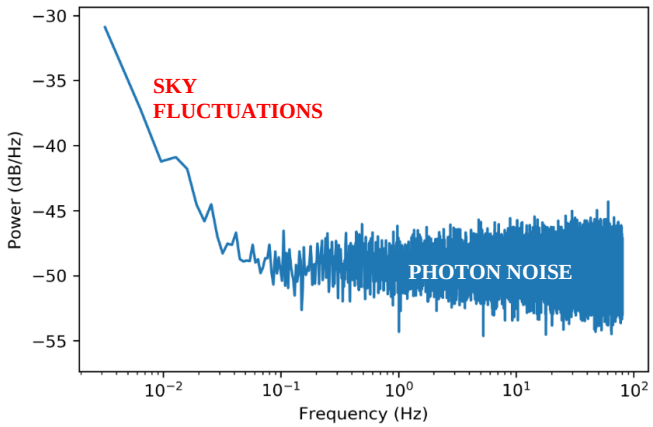

Figure 2.4: Power spectrum of sky temperature output of TiEMPO, showing sky fluctuations and photon noise.

2.2.2 Noise sources due to detection & measurement

There are also two noise sources which are considered relating to the detection of a signal by a KID, and the measurement of the signal at the readout. These sources are the two-level system (TLS) noise [10], and the analogue-to-digital converter (ADC) noise.

Two-level systems exist in the substrate material of the detector, and the fluctuations of these TLSs leads to a fluctuation in the resonant frequency of the KIDs [10], hence causing noise in the domain of the KID frequency, δx. The ADC noise relates to the conversion of the analogue signal received from the KID, to a digital signal to be read out. The finite number of bits used when digitising leads to this noise source. The digitisation is performed on the carrier signal, hence the ADC noise is introduced at the carrier [11].

TLS and ADC noise share similarities with sky and photon noise. TLS noise, similarly to sky noise, has a frequency dependence, and will have a $1/f$ shape in the power spectrum, whilst ADC noise is also flat in the power spectrum, similarly to photon noise. Hence, the combination of TLS and ADC noise will produce a similar spectrum as in **Figure 2.4**, albeit at different levels. The aim for the development of the KID model is to therefore include these noise sources as the signal is being passed through.

3 Development of KID model

3.1 KID Model from temperature

In order to utilise the output of the sky simulator, the KID model equations defined earlier in Section 2 can be used in combination with other theory to describe how a KID would respond to a particular load.

3.1.1 Conversion to KID parameters

In the paper by Takekoshi et al. [4], a model is formulated which relates the normalised frequency shift δx (as described in Section 2) of a KID, to the optical loading temperature T:

$$\delta x = p_0\left(\sqrt{T + T_0} - \sqrt{T_{load} + T_0}\right) \tag{3.1}$$

T is the effective black body temperature of the optical load seen by the KIDs, and T_{load} is the reference room-temperature (300K) load used for the calibration of the KIDs. The parameter p_0 represents a proportionality factor determined by the KID sensitivity, and T_0 is a constant correction term: $T_0 = -\frac{h\nu}{2k_b}$ ($= -8.4$ K at 350 GHz) [4]. Since the model assumes a linearity between power and temperature (Rayleigh-Jeans), this correction term is needed to get a closer fit to Planck curve. The model produced very good fits to observed data using a sky dip, a change in the elevation of the telescope to change the sky transmission and effective sky temperature T_{sky}, as can be seen below in **Figure 3.1**:

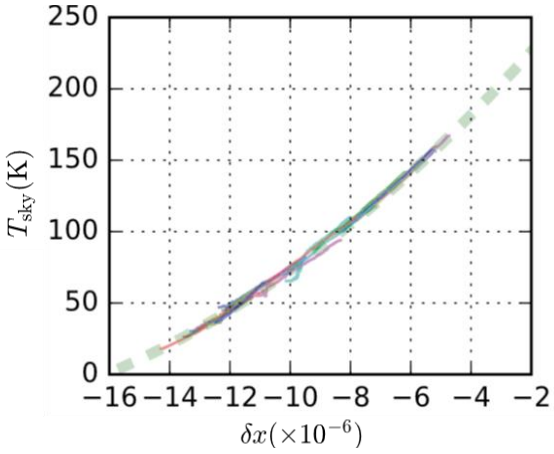

Figure 3.1: Plot from Takekoshi et al., showing the fit of the observations to their model [4].

While T_0 is a constant, p_0 is filter/frequency dependent. Takekoshi et al. calculated the values for each filter, the plot of which is shown below in **Figure 3.2** [4].

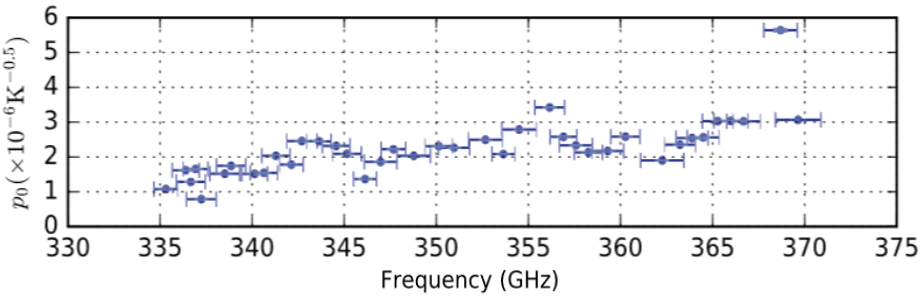

Figure 3.2: Plot from Takekoshi et al. [4], showing filter dependence of p_0

Given the description of the parameter X, as defined earlier in Section 2, this can be inserted into **Equation (3.1)**. Therefore, the equation in terms of X is given by:

$$X = 2Q_L p_0 \left(\sqrt{T + T_0} - \sqrt{T_{load} + T_0}\right) \tag{3.2}$$

Since the output temperature of the sky simulator is the sky temperature, T_{sky}, it needs to be multiplied by the forward efficiency in order to give the optical loading temperature: $T = \eta_{fwd} T_{sky}$[1].

The relationship between X and phase defined earlier can then be combined with **Equation (3.2)** above to convert from temperature to phase, hence enabling the ability to use the output signal of the sky simulator to give a signal in KID phase.

3.1.2 Responsivities

Observing the relative responsivities of various parameters is a useful tool, therefore this sub-section will describe these responsivities. The responsivity of the phase to the frequency parameter is given by:

[1] This is the way it was implemented in the results. On reflection, this was likely an error, as the forward efficiency was already taken into account in the simulation with TiEMPO, hence did not need to be considered again.

$$\frac{d\theta}{dX} = \frac{2}{X^2 + 1}$$

(3.3)

The responsivity of the KID phase to the temperature ($d\theta/dT$) then needs to be formed. This is done through the chain rule, using the expressions for the phase responsivity to the frequency parameter X, and the responsivity of X to temperature absorbed by the KID [12]:

$$\frac{d\theta}{dT} = \frac{d\theta}{dX} \times \frac{dX}{dT}$$

(3.4)

The expression describing the frequency-temperature relation can be differentiated in terms of T to obtain $\frac{dX}{dT}$:

$$\frac{dX}{dT} = \cancel{2}Q_L p_0 \left(\frac{1}{\cancel{2}}(T + T_0)^{-\frac{1}{2}}\right)$$

$$\frac{dX}{dT} = \frac{Q_L p_0}{\sqrt{T + T_0}}$$

(3.5)

The chain rule is then employed to give $\frac{d\theta}{dT}$ as:

$$\frac{d\theta}{dT} = \frac{2Q_L p_0}{\sqrt{T + T_0}(X^2 + 1)}$$

(3.6)

This is perhaps more helpful to write entirely in terms of T, but the equation becomes less clear, hence it is left as above, since the two effects which dominate the responsivity can clearly be seen in the denominator: the $1/\sqrt{T}$ dependence, and the Lorentzian $1/(X^2 + 1)$.

3.2 Adding noise sources

To complete the model of noise at measurement, the noise sources between the receipt of the radiation at the KID and the measurement at the readout need to be added. These are the TLS and ADC noises as described earlier in Section 2.

3.2.1 Generating noise sources

The main challenge was with generating the TLS noise, in particular creating the correct $1/f^n$ shape in the power spectrum and setting the desired level at the desired frequency. The procedure for generating the TLS noise was to first generate white noise at a particular level. In general, the level of the TLS noise is defined as a level at a particular frequency. Hence, the white noise level generated is the level at this particular frequency. Therefore, the initial step of generating TLS noise is essentially the same as the generation of ADC noise.

The white noise is generated by using a random number generator in Python, which uses a normal distribution. The white noise level is determined by the standard deviation value of the noise generated, and is given by **Equation (3.7)**, where PSD_{val} is the desired level of the power spectrum, and $f_s/2$ is the bandwidth (half of the sampling frequency).

$$\sigma = \sqrt{\frac{f_s \times PSD_{val}}{2}} \tag{3.7}$$

This white noise is generated in the time domain, which is then Fourier transformed to give the noise in the frequency domain, from which the power of the noise in the frequency domain could be determined. An example of the power spectrum of generated white noise is shown in **Figure 3.3 a)**.

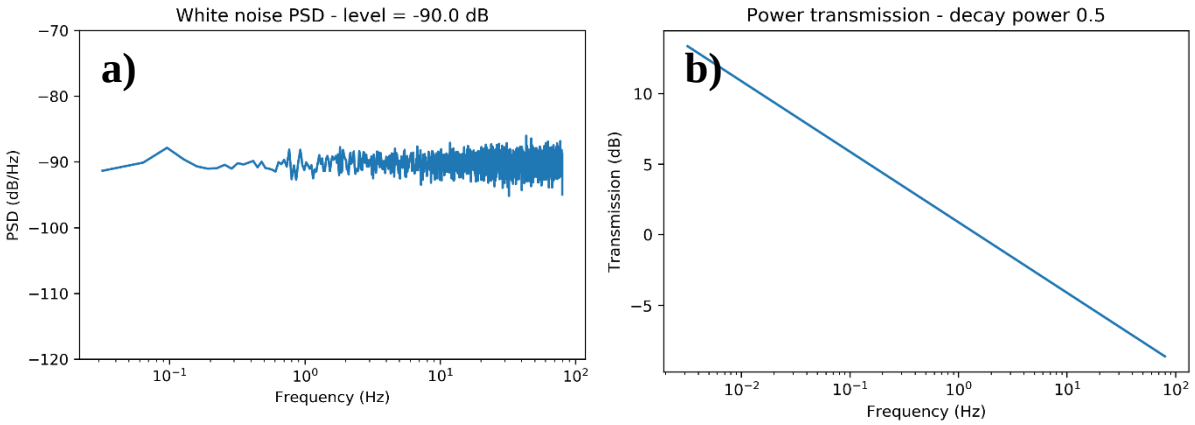

Figure 3.3: a) Example white noise generation, and **b)** Example transmission filter

In order to then create the $1/f^n$ shape, and set the frequency at which the TLS noise reaches the level above, a transmission filter was used. The transmission value at each frequency was simply the inverse of the frequency to the desired power. The filter is multiplied by the white noise in order to give the desired 1/f shape. White noise is chosen to generate the TLS noise since it is desirable to have noise in the spectrum, and random values of phase, such that a realistic noise source is generated.

The filter shape is set in power, since that is where the characteristics are known, however the multiplication takes place in amplitude, which has the full complex information of the spectrum, as it is the complex Fourier transform of the time stream. Hence the square root of the filter shape defined in power is used in the multiplication. An example filter shape (in power) is shown in **Figure 3.3 b)**.

Finally, in order to get the TLS level at the desired frequency, the transmission values of the filter were normalised by f_{knee} (the desired frequency), such that the transmission value would equal 1 at f_{knee}. This ensures that when the white noise is multiplied by the filter, the overall $1/f^n$ shape will reach the white noise level at f_{knee}. The overall equation of the transmission filter is as shown in **Equation (3.8)**. **Figure 3.4** shows the result of the TLS noise generation, with the flat white noise also shown to illustrate the crossover at f_{knee}.

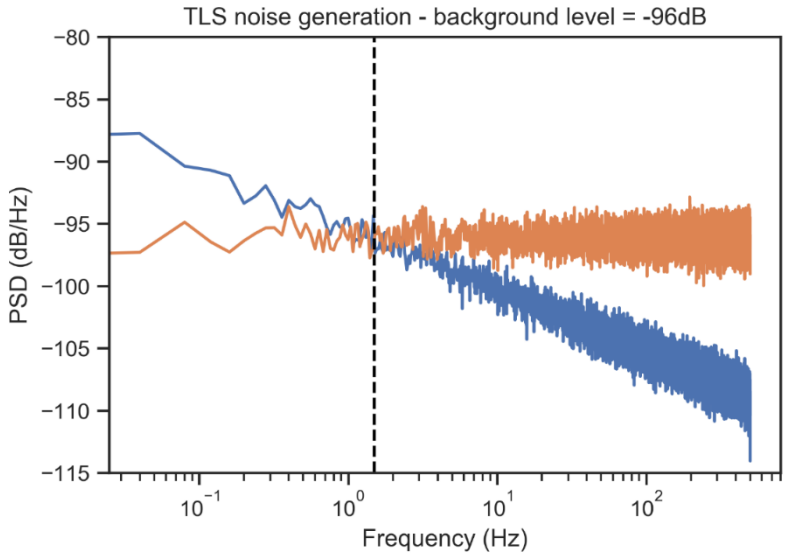

Figure 3.4: Example of result of TLS noise generation, setting the level at -96 dB at 1.5 Hz. Orange curve shows white noise, to illustrate crossover. Black dotted line set at 1.5 Hz separately

$$q(f) = \left(\frac{f}{f_{knee}}\right)^{-n}$$

(3.8)

It should be noted at this point that there was a certain breakdown of the 1/f noise generation at high decay powers (2 and above). The effect was noted when using a data smoothing method, in this case the Welch method, which caused the noise levels at a given frequency to depend on the timestream length. However, for the range of values of interest for the model, the generation of the TLS noise was checked, and found to function well without causing serious problems. Therefore, this method was deemed sufficient for usage.

The TLS noise generation is finished in the frequency domain, after which it is inverse Fourier transformed back to a time stream. The ADC noise is simply generated in the time domain using **Equation (3.7)**.

3.2.2 Adding the noise

Since the noise sources affect different domains, each is generated in the domain which they affect before being added to the time stream of the data. The ADC noise is generated in terms of the carrier, but added in KID phase (θ), whilst the TLS noise is generated in terms of the KID frequency (δx), and is added in the X-domain. (Note that for the preliminary results with DESHIMA 2.0 data, the TLS noise is generated and added in terms of X).

Therefore, when setting the desired levels of the noise sources, the relative levels between different domains need to be considered. In the equations below, the relative PSDs of different domains are shown.

$$PSD_\theta = PSD_{\delta x}\left(\frac{\partial\theta}{\partial\delta x}\right)^2 \sim PSD_{\delta x}(4Q)^2, \ \theta \to 0$$

(3.9)

$$PSD_c = PSD_\theta\left(\frac{1 - S_{21}^{min}}{2}\right)^2$$

(3.10)

Given that the TLS noise is generated and added in terms of KID frequency, in order to get the desired level at KID phase the value will have to be adjusted according to **Equation (3.9),** when generating in KID frequency. Since it is added in terms of X, it also needs to be multiplied by $2Q_L$.

As for the ADC noise, since it is added in KID phase but generated in terms of the carrier, it will have to be divided by the normalisation factor $\left(\frac{1-S_{21}^{min}}{2}\right)$, when it is added to the KID phase time stream. The flowchart in **Figure 3.5** summarises the process of converting from T to θ, while adding noise.

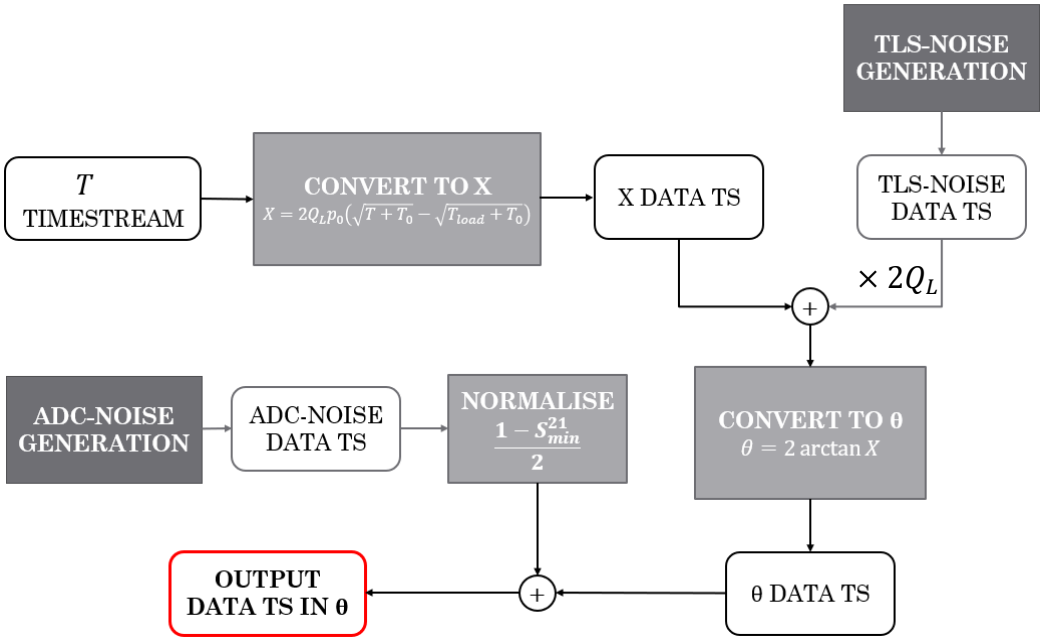

Figure 3.5: Flowchart showing procedure of converting temperature to phase, whilst adding TLS and ADC noise sources

4 Preliminary testing & results for DESHIMA 2.0

In order to evaluate the model, the data output from the sky simulator was used in combination with the KID model. This data was the simulated sky temperature for an observation with the DESHIMA 2.0 instrument. This section will describe the parts of the data chosen, some key assumptions made in the usage of the model, and the results obtained.

4.1 Data & Assumptions chosen

4.1.1 Data

As mentioned previously, the data used was from a simulation of an observation by DESHIMA 2.0. The simulation was for a full night's observation, i.e. roughly 8 hours, divided up into 8 files, and the simulation was performed for 5 sky positions, as shown in **Figure 4.1** below [2]. Position 2 (in the middle) represents the on-source position, with the rest off-source. The pointing angles between the positions is such that, in the near-field (the atmosphere), they are almost entirely overlapping, but in the far field (the source), they are entirely separate. Thus, there should be no loading from the source in the off-source positions.

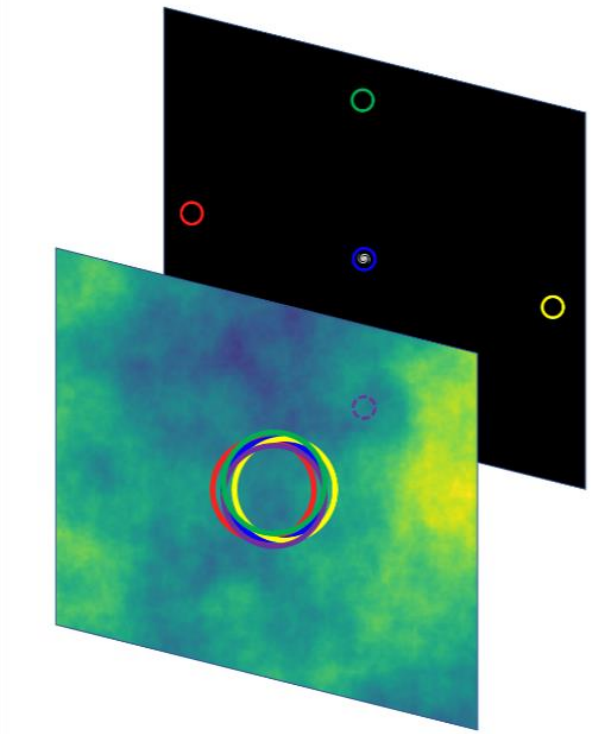

Figure 4.1: Illustration of five chopping positions, with position 2 being centre and on-source [2]. The positions are indicated both in the near-field of the telescope and atmosphere, and the far-field for astronomical sources.

Additionally, DESHIMA 2.0 had 347 spectral channels, **Figure 4.2** below shows the mean temperature in each filter.

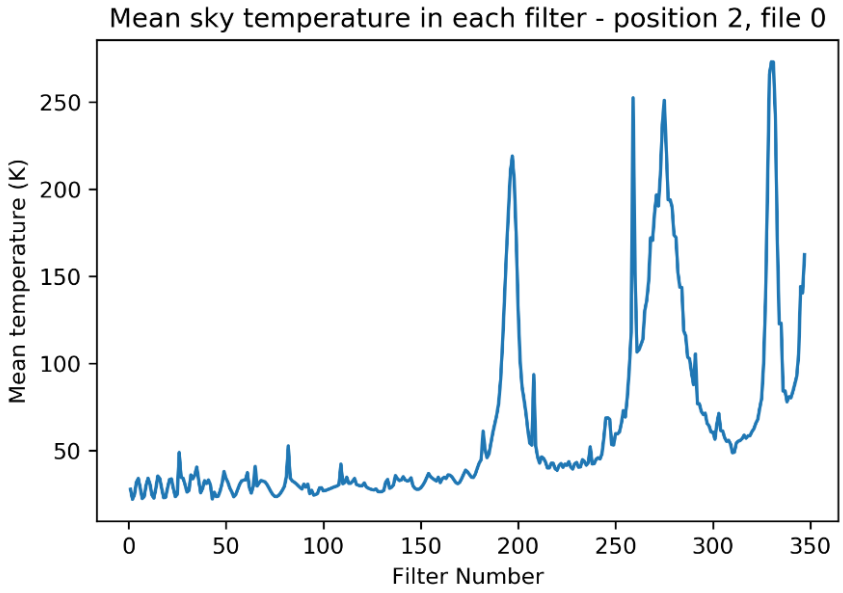

Figure 4.2: Example of mean sky temperature of each filter from simulation data

The decision was subsequently made to use only the data from the first file (file 0), corresponding to roughly an hour of observation. Additionally, based on the figures above, it was decided to use position 2 and filter number 220 to validate the model.

4.1.2 Model values

The initial data possessed was for a simulation of DESHIMA 2.0, so it was not possible to use actual values for the detector parameters, since these were not available for DESHIMA 2.0. Therefore, constant assumed values were used for these parameters.

A couple of aspects of the model as described in the previous section were not used, or were changed. The correction parameter T_0 was neglected (only for the DESHIMA 2.0 results), as it was felt this would not affect results significantly, and the forward efficiency was not used on the sky temperature. Additionally, as mentioned earlier, the level of the TLS noise was set in terms of X rather than in terms of δx. As for the rest of the model parameters, the values were assumed, with an overview of the initial assumed values shown in **Table 4.1**.

Parameter	*Assumed value*	*Notes*
Q_i	60,000	
Q_c	15,000	
p_0	2×10^{-6}	Initial. Chose reasonable value from **Figure 3.2**.
PSD_{TLS}	-96 dBx/Hz	Set at -96 dBx, in order to get -90 dBk
PSD_{ADC}	-100 dBc/Hz	
T_{load}	300 K	Initial value, corresponding to room temperature load from Takekoshi et al. [4]

Table 4.1: Summary of initially assumed model parameters. dBx, dBk, and dBc refer to the value in decibels in X, the KID phase, and the carrier, respectively.

4.2 Results

4.2.1 Results with initial parameters

With the original values as shown above, a set of spectra was made. The sky temperature data was passed through the KID model to the KID phase, adding the TLS and ADC noise sources, to form the full time stream in KID phase. Additionally, in order to view the various contributions, the sky temperature data is converted to KID phase without adding the noise sources. The two KID noise sources are then also individually converted to KID phase. The resulting plot of all four is shown below in **Figure 4.3**.

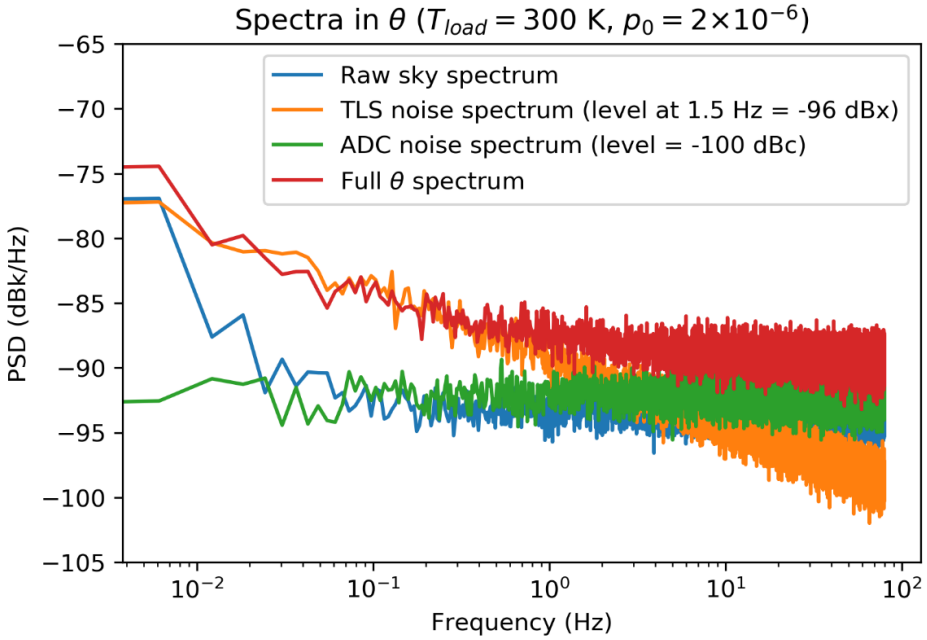

Figure 4.3: Spectra in KID phase, showing contributions of each noise source to the overall noise spectrum

4.2.2 Analysis & changes

In the figure above, showing all of the spectra, it can be seen that the noise from the sky and photon noise is comparatively low. At low frequencies, the overall noise spectrum is dominated by the TLS noise, the level of which is significantly higher than the rest for the low frequencies. It was expected that the overall spectrum would be mainly dominated by the noise due to the atmospheric fluctuations and photon noise.

The significantly lower photon noise level was considered to be caused by the higher efficiency and sensitivity of DESHIMA 2.0, and so using the detector parameters of DESHIMA 1.0 caused a lower photon noise level. The issue therefore appeared to be due to the assumptions of the parameters, with the biggest influence being p_0, which affects the responsivity of the model.

This is well summarised in **Figure 4.4** below. The responsivity for temperatures ranging from 10-400K was calculated using the temperature to phase responsivity formulation in **Equation (3.6)**. This was then also done for various values of p_0, to observe the effect on the responsivity.

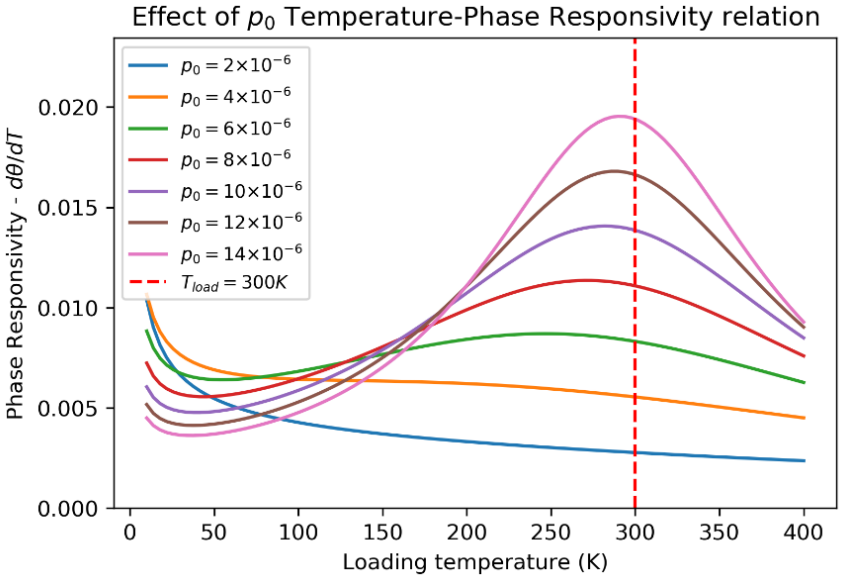

Figure 4.4: Plot showing the effect of p_0 on the responsivity of model, for a temperature range of 10-400K (T_{load} = 300K)

The plot shows the two behaviours present in the responsivity equation: when p_0 is low, the responsivity is low, and the $1/\sqrt{T}$ dependence is seen. For higher p_0 values, there is a

greater responsivity, and the Lorentzian form of the KID is more clearly visible near resonance. The p_0 value chosen earlier (2×10^{-6}), is relatively low, so an increase in the value can correspond to a significant increase in the responsivity.

It was consequently decided to run the model and produce the spectra with an increase in value for p_0 to 8×10^{-6}. The original value chosen was based on the plot from the paper by Takekoshi et al. (**Figure 3.2**) [4], which was for DESHIMA 1.0. In order to account for the large increase in the efficiency for DESHIMA 2.0, a value four times greater was estimated [6].

An issue to address first was the dynamic range. For the value of $p_0 = 2 \times 10^{-6}$ there is a large dynamic range of temperatures that can be used, given that temperatures a fair way off resonance do not cause a large change in the responsivity, and so the KID does not need to be calibrated close to the expected temperature. At higher p_0 values, the Lorentzian provides a significant increase in the responsivity, but a lower dynamic range, so this increased responsivity is only particularly significant close to resonance, i.e. when the temperature values are close to T_{load}.

T_{load} would therefore have to be chosen such that the KID would remain close to resonance. This was done simply by making T_{load} equal to the mean temperature of the filter. In the case of filter 220, this value was 38.54K. The implication of this was therefore that in the usage of DESHIMA, the calibration would need to be based on the sky temperature. The resulting plot of the spectra for $p_0 = 8 \times 10^{-6}$ and $T_{load} = 38.54$ is shown below in **Figure 4.5**.

The plot shows that the noise level of the sky and photon noise has significantly increased, to the point where the overall spectrum is almost entirely dominated by these noise sources. Naturally, this run of the model makes the assumption that it is very close to resonance, which requires an intensive calibration scheme, nevertheless the desired effect was still achieved.

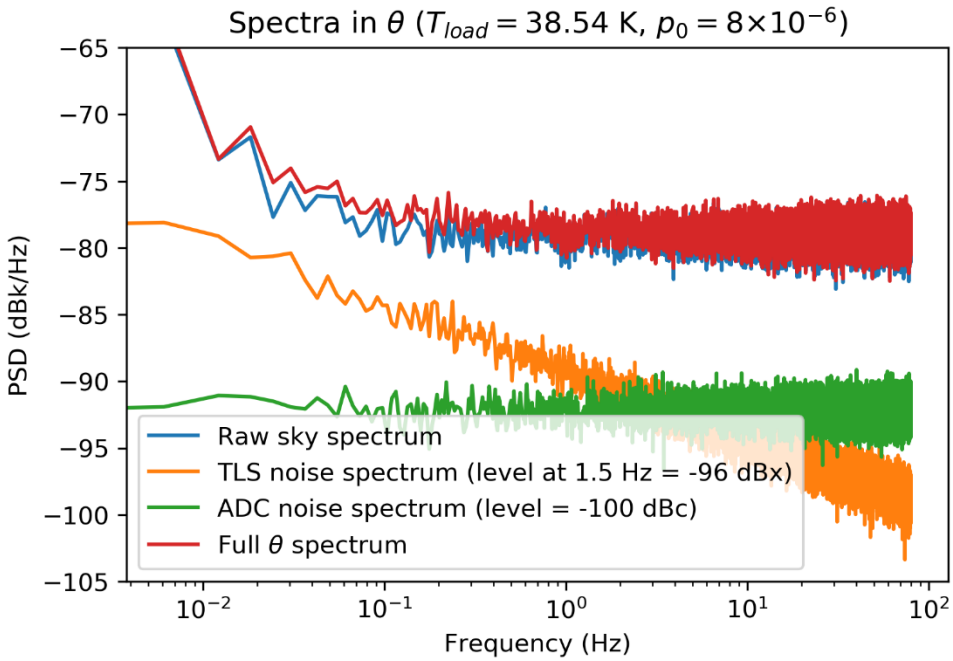

Figure 4.5: Spectra in KID phase, showing contributions of each noise source to the overall noise spectrum

In the end however, it was decided that simply adjusting the value of p_0 was insufficient. The detector and instrument parameters used in the model are not present yet for DESHIMA 2.0 and constant assumed values needed to be used. It was decided that it would be more useful to use TiEMPO to simulate an observation for DESHIMA 1.0. There was not only plenty of detector-specific data available to use for the detector parameters of DESHIMA 1.0, but there was also real observation data taken by DESHIMA 1.0. Consequently, running the simulation and the model for DESHIMA 1.0 would have the advantage of being able to compare to real observation data, using specific detector parameters for each KID, rather than constant assumed values. This would lead to increased accuracy in the results and greater analytical capabilities.

5 Simulation with DESHIMA 1.0

The code for the simulator was adapted by Esmee Huijten to include the possibility of running the simulator with DESHIMA 1.0 settings. In the simulations described in this report, certain values were changed in the code to correspond with the observation data.

5.1 Parameter settings for DESHIMA 1.0

5.1.1 Efficiencies

The main significant settings that needed to be changed were the various efficiencies in the instrument. **Table 5.1** below summarises the various efficiencies, with their description from the code of the DESHIMA model [2].

Efficiency	***Description***
eta_M1_spill	Spillover efficiency of primary mirror
eta_M2_spill	Spillover efficiency of secondary mirror
eta_wo_spill	Product of all spillover losses in the warm optics in the cabin
eta_co	Product of: Cold spillover Cold Ohmic losses Filter transmission
eta_lens_antenna_rad	The loss at chip temperature, *that is not in the circuit.* Product of: Front-to-back ratio of the lens-antenna on the chip Reflection efficiency at the surface of the lens Matching efficiency, dur to mismatch Spillover efficiency of the lens-antenna
eta_circuit	The loss at chip temperature, *in the circuit.* Defined as eta_filter_peak multiplied by Lorentzian shape across filters
eta_IBF	in-band fraction efficiency
eta_opt	Optical efficiency for DESHIMA 1. Inserted into model code, product of **eta_co*eta_lens_antenna_rad*eta_circuit*eta_IBF**. eta_opt used, and the four efficiencies set to 1.
eta_mb	main beam efficiency
eta_M1_ohmic, eta_M2_ohmic	Ohmic losses, same for both mirrors, given by eta_Al_ohmic (function of frequency). Unchanged.
eta_M1	Calculated from: eta_M1_ohmic * eta_M1_spill
eta_wo	Calculated from: eta_Al_ohmic**n_wo_mirrors (number of warm-optics mirrors) * eta_wo_spill
eta_chip	Calculated from: eta_lens_antenna_rad * eta_circuit*eta_opt. (factor of eta_opt included here)

Table 5.1: Descriptions of the efficiencies in the code of TiEMPO [2]

The key change to mention is the inclusion of the optical efficiency, which was the efficiency between detection and the cryostat window. It is defined as the product of four efficiencies, therefore in the code these four are set to 1, and the optical efficiency is included. The optical efficiency is included as an extra factor in the calculation of eta_chip. This is preferred as an efficiency parameter because it is a known and measured value.

The value was obtained from a data file containing the values for each KID. The plot of these values is shown in **Figure 5.1** below [13]. However, only one value was used in the code, so the mean of the values between 350-370 GHz (roughly the flat part) was taken.

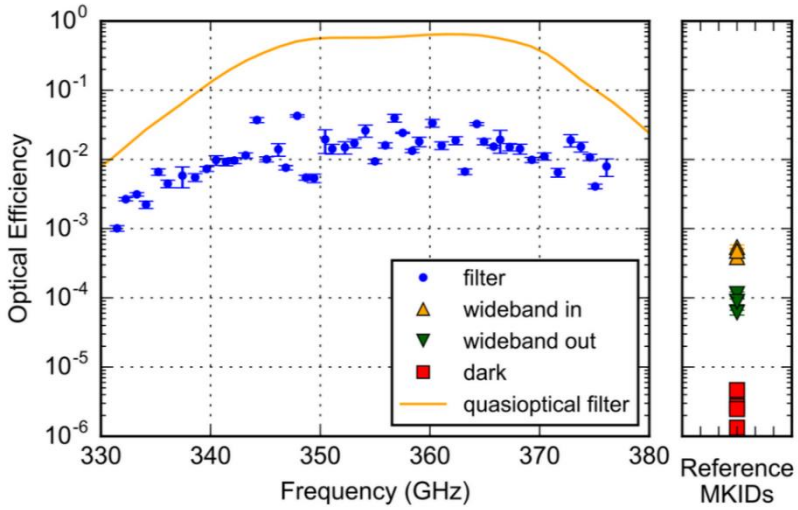

Figure 5.1: Plot of optical efficiency values for each KID [11]

5.1.2 Filters and Splines

Naturally, the filter frequency values for DESHIMA 1.0 would be different to DESHIMA 2.0, therefore these needed to be changed in the code. Given that the actual filter frequencies were obtained from the DESHIMA database fits file, the definition of the filters needed to be changed. In the code, the filters were ranged from minimum to maximum frequency. This was changed to define all the filter frequencies as an input, so the frequencies from the fits file could be used. The spectral resolution was kept constant at 300, which is valid as work is done in temperature, and the bandwidth affects the power to temperature conversion.

The change in the filter frequencies necessitated a change in the splines used to convert between power at the KID and T_{sky}. The sky simulator would calculate, using the efficiencies

above and radiative transfer, the power absorbed by the KID. This power was then converted back to sky temperature by the use of splines, which were defined at each filter frequency for DESHIMA 2.0. Due to the change in both the efficiencies and the filter frequencies, these spines needed to be created anew for DESHIMA 1.0. This was done by running the function 'filterbank.py' using the new definition of the filters.

5.2 Simulations

5.2.1 Procedure

The procedure for simulation involved running in the script 'main.py', which would essentially run the simulation by calling 'signal_transmitter.py', which transmitted the signal through the components of DESHIMA, and saved the generated sky temperature data.

In 'main.py' certain key parameters of the simulation could be set, for example the atmospheric settings, the simulated galaxy values, and the observation time. These could be modified depending on what needed to be simulated. The desire in this project was to replicate an observation performed by DESHIMA 1.0, which has the run ID 1318. This was a 1-hour still-sky observation with the pointing constant in elevation and azimuth at an elevation of 88 degrees, taken in 2017, with the precipitable water vapour value of 1.72mm. Additionally, in 'signal_transmitter.py' the task is divided into a number of jobs which run in parallel, so that simulation time will be reduced. The number of parallel jobs was set at 20, due to computational availability. **Table 5.2** summarises the observation settings used.

Parameter	***Description***	***Setting***
pwv_0	Precipitable water vapor of observation	1.72mm
windspeed	Wind speed	10 m/s
prefix_atm_data	Atmosphere data used	'aris200602.dat-' (numbers are date stamp)
EL	Elevation angle	88^0
obs_time	Duration of simulated observation	3600s (1 hour)

Table 5.2: Summary of observation settings for DESHIMA 1.0 simulation

The filter values from the fits file were also loaded in at 'main.py'. Using the above settings, a simulation of a 1-hour observation by DESHIMA 1.0 was performed.

5.2.2 Initial results & changes

In order to evaluate how well the simulation managed to replicate an actual observation, spectra were created. The output T_{sky} data from the simulation was passed through the KID model, with the TLS and ADC noise sources added, to give the data in KID phase. The power spectrum of this data was then made using the Welch function to smooth the data.

The KID model parameters used (p_0 and Q-factors) were obtained from fits files, which contained information about these parameters for each KID. Then, depending on the KID being analysed, these parameters could be extracted and used. The KID chosen for initial analysis was number 38, which had the master ID of 130. This was because it had an optical efficiency value close to the one used for the simulation. Since there was a fair amount of variation in the value of the optical efficiency, but a mean value was used, it was deemed useful to use a KID which had a value close to the value used in the simulation.

The fits files also contained the amplitude and phase data collected from the observation. The power spectrum of the phase data was also made using the Welch method, and the two spectra were plotted together in order to compare them. An example from KID 38 is shown in **Figure 5.2**. As can be seen from the figure, there were clear differences between the spectra that needed to be addressed. These differences were present despite the TLS and ADC noise levels being set based upon the real observation spectrum. If these differences could be traced to a cause, which could then be justifiably adjusted, then this could perhaps help to form a realistic replication.

Firstly, the white noise level of the simulated data was too low, with around 3dB in the plot above indicating a possible factor of 2 which was causing issues. It was however eventually found that there was a fair amount of scatter in the white noise level between the KIDs, and

although there was frequently a difference, there did not seem to be a specific 3dB (or factor of 2) offset.

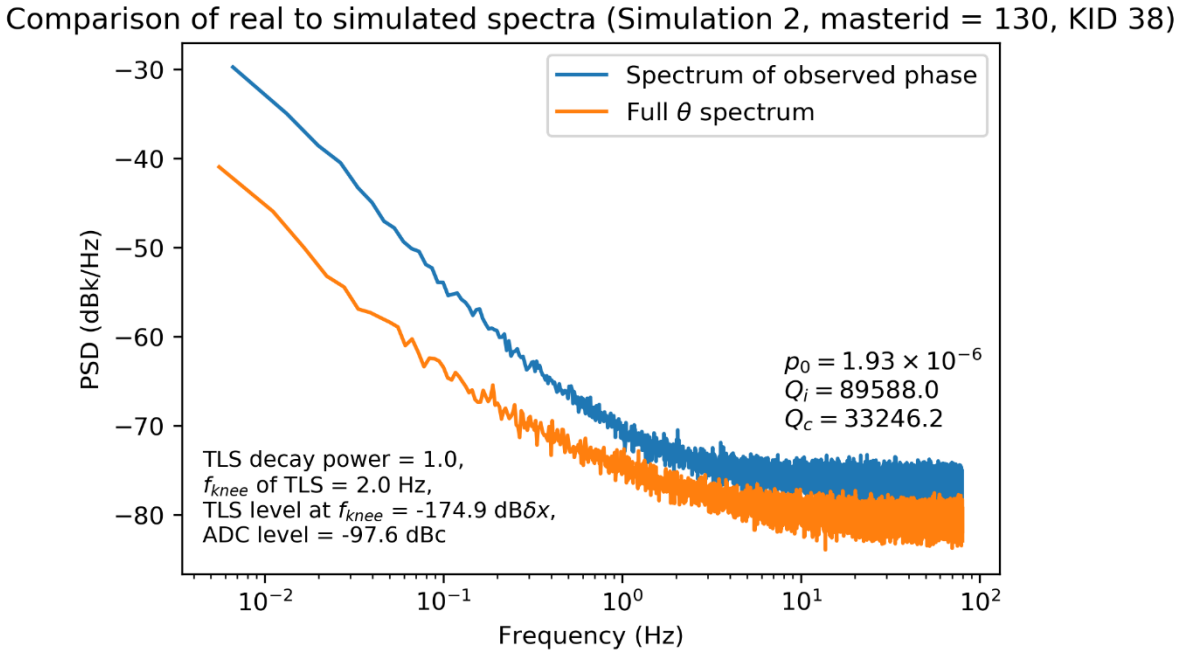

Figure 5.2: Comparison of observed and simulated spectra for KID 38. TLS and ADC levels were set according to characteristics of observed data spectrum

During the search for a possible reason for the white noise offset, it was found that the forward efficiency was not taken into account in the warm optics spillover, i.e. eta_wo_spill. This was therefore changed from 0.99 to 0.86, to reflect the forward efficiency of DESHIMA 1.0. This corresponds to a significant change, given the warm optics are at 300K, leading to an additional temperature load of $(0.13 \times 300) = 39$ K, which in turn affects the photon noise level.

The shape of the $1/f^n$ noise caused by the sky fluctuations was also not quite matching. The slope was greater, and the level was higher in the data of the real observation. Therefore, a new, shorter (15 minutes) simulation was performed, changing the eta_wo_spill value, and windspeed to 20m/s in the hope of increasing the white and $1/f^n$ noise, respectively.

The new simulation did not affect the $1/f^n$ noise as had been hoped, the slopes still did not quite match. It also did not affect the white noise level significantly, although this was not deemed a specific issue, given the scatter in the differences.

5.2.3 Final settings

Having seen that that the $1/f^n$ shape was still not quite matching, the decision was made to change the atmosphere data to attempt to change the $1/f^n$ noise. The atmosphere data was produced by ARIS [3], which previously used an RMS value of 50 μm. It was deemed justifiable, since the pwv value was higher at 1.72mm (compared to 1.0 mm), to increase this RMS value to 150 μm, which was expected to give a better match to the $1/f^n$ noise.

Hence, new atmosphere data was produced with this RMS value (many thanks to Akira Endo), and this atmosphere data was used in the final simulation of a full 1-hour observation. The observation settings for this final simulation are shown below in **Table 5.3** (the windspeed was returned to 10 m/s as it did not seem to have an effect).

Parameter	***Description***	***Setting***
pwv_0	Precipitable water vapor of observation	1.72mm
windspeed	Wind speed	10 m/s
prefix_atm_data	Atmosphere data used	'aris200622.dat-' (new atmosphere data with RMS=150 μm)
EL	Elevation angle	88^0
obs_time	Duration of simulated observation	3600s (1 hour)

Table 5.3: Summary of settings used for final DESHIMA 1.0 simulation

The efficiencies used for the final simulation are shown in **Table 5.4** below, which were approximated from values for DESHIMA 1.0 [6] [13].

Efficiency	***Value***
eta_M1_spill	0.99
eta_M2_spill	0.6
eta_wo_spill	0.86
eta_co	1
eta_lens_antenna_rad	1
eta_circuit	eta_filter_peak set to 1
eta_IBF	1
eta_opt	0.0183 (Mean of values between 350-370 GHz from data)
eta_mb	0.34
eta_M1_ohmic, eta_M2_ohmic	Defined as same function in code
eta_M1	Calculated, not set
eta_wo	Calculated, not set
eta_chip	Calculated, not set (eta_opt included here)

Table 5.4: Efficiency values used for final simulation

This simulation appeared to show more expected results, discussed further in the next section. A log of all the simulations performed can be found in **Appendix A**. There it can be seen what precise changes were made, and the settings for which the simulations were run.

6 Results & Analysis

6.1 Spectrometry

The data used here is the raw T_{sky} data from the simulation using TiEMPO, therefore this section analyses the data that goes into the KID model. The data which has the KID noise sources added could have also been used, but they would be subtracted in any case when doing on-source minus off-source subtraction. A realistic chopping strategy could be implemented in the future.

Firstly, to characterize the data fed into the KID model, it is useful to plot the mean temperature in each filter, to see the spectral information at the KIDs. **Figure 6.1 a)** below shows the mean temperature across the filters. The general shape of this plot appears to match with the plot of the NEFD and a galaxy observation shown in **Figure 6.1 b)** [2]. This indicates that the mean temperature plot is reflecting the filtration of the signal by the atmosphere.

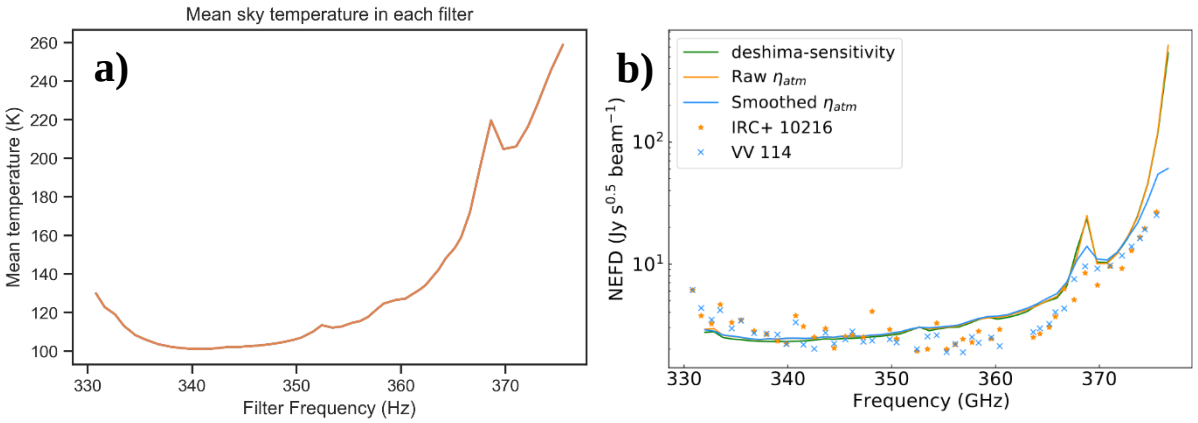

Figure 6.1: a) Plot of mean temperature across filters, **b)** NEFD of simulation in [2] along with observation data of galaxy VV114

Additionally, it is interesting to view the mean temperatures of the on-source position minus the mean temperatures of an off-source position, in order to try to observe emissions from a source. **Figure 6.2** below shows the results, using position 3 as off-source (Python indexed as 2).

An issue to note is the on minus off source mean temperatures when position 5 is used as the off-source position. The shape of the curve across filters appears to be flipped, and the

values are negative. This is shown in **Figure 6.2 b)**. The reasons for this are possibly due to the differences in time and elevation between the positions. The time delay is caused by the wind direction. This is entirely hypothetical at this point, and investigating further is beyond the scope of this project. One feature is present in the same way in both plots, which is the spike at 350 GHz. This is a spike in both plots, even though the second plot appears to be flipped. This seems to indicate that this is a feature rather than the general variations.

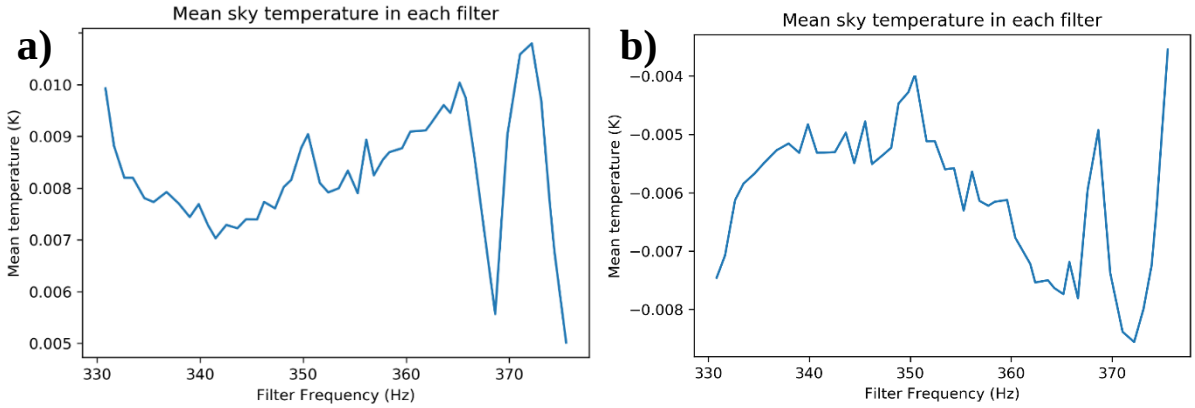

Figure 6.2: Mean of on-source minus off-source temperatures. **a)** Off-source position 3 (2 in Python index) **b)** Off source position 5 (4 in Python index)

Due to the fact that position 5 was at a different elevation, it was decided that it would be better to use the average of positions 1 and 3 as the 'off-source position'. The result is shown below in **Figure 6.3**.

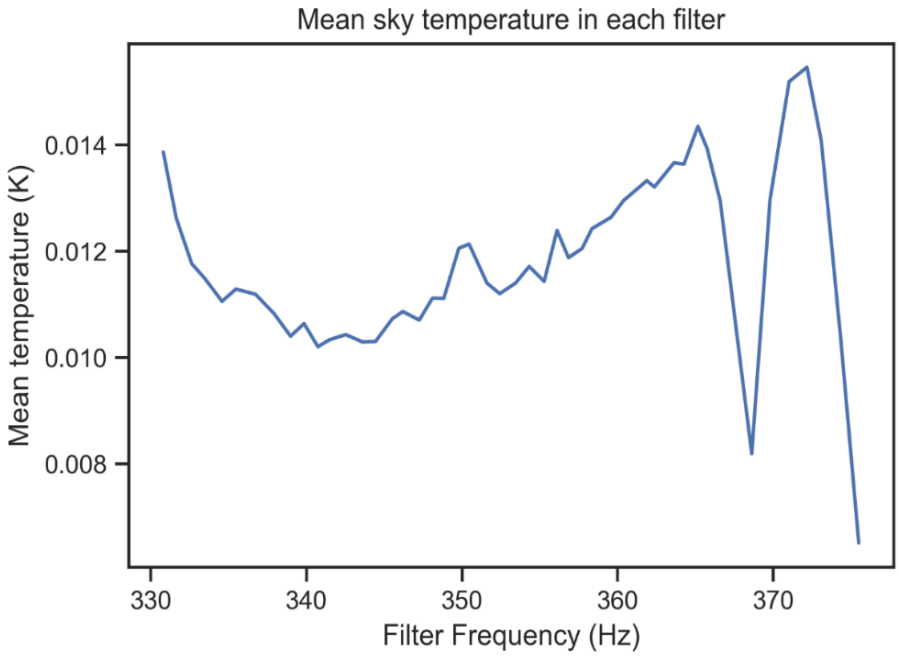

Figure 6.3: Mean sky temperature with on-off subtraction. Off position is a mean of positions 1 and 3

The plot shows a similar shape, with the values being both positive, and of a greater magnitude. The feature is still present; although it appears smaller, it is still the same size, but is relatively smaller given the larger overall magnitude. **Figure 6.4** below shows a simulated galaxy spectrum using the spectrum creation function in TiEMPO, for the frequency range of DESHIMA 1.0. The properties of the galaxy were set the same as for the simulation: redshift=4.43, luminosity=13.7, linewidth=600.

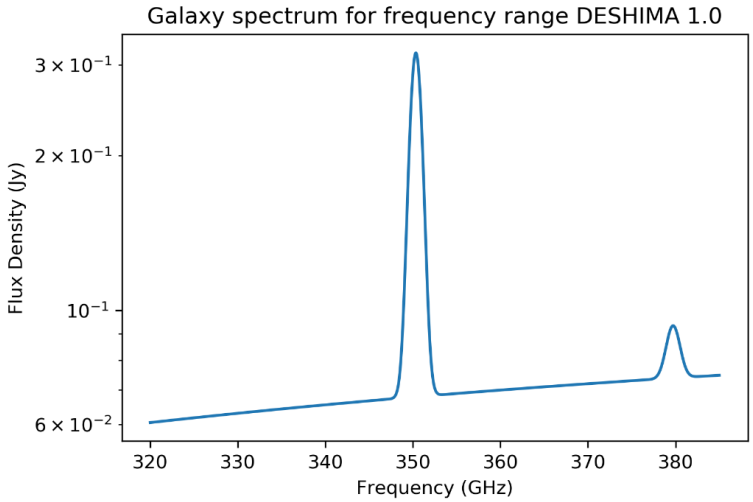

Figure 6.4: Simulated galaxy spectrum created using the corresponding function of TiEMPO, for the frequency range of DESHIMA 1.0. The galaxy properties were: redshift=4.43, luminosity=13.7, linewidth=600

The plot shows that there is an emission line present at 350GHz. Therefore, given that the spike in **Figure 6.2** is present in both plots, it appears that this spike reflects the emission line of the simulated galaxy. The relative heights of the emission line and the feature indicate that the sensitivity of the instrument in the simulation was around 230 Jy/K, which is comparable to what is observed [6]. These plots indicate that emission lines/peaks can indeed be observed, but the observation of continuum emission appears to be very difficult, given that there seems to be some of the sky left over after the subtraction, using a simplified chopping.

6.2 Spectra

The spectra of the data in KID phase are particularly useful to observe, as the noise from the sky, photon, TLS and ADC sources can be observed, and the simulation and the KID model can then be analysed. In using the KID model, values for the TLS and ADC noise sources

needed to be set. In general, these values are shown on plots for which they are relevant. The process by which they are selected are as follows.

The f_{knee} of the TLS noise is consistently set at 2 Hz, which is the point at which it will reach the "TLS level". This level was meant to be constant in the δx domain for all KIDs (since the Q-factor would not be an issue). Hence this level for each KID was found by identifying the white noise level of the observed phase PSD, and dividing by $(4Q)^2$ to convert to δx (see Equation **(3.9)**). The mean value across all the KIDs was found to be -174.9 dBδx/Hz, which was then used whenever setting the "TLS level". The slope of the TLS noise (n in $1/f^n$) was set at 1 in power. At low frequencies the slope is not well known, but this power best matches observed data. The ADC level on the other hand, was calculated and set individually for each KID, by calculating the white noise level of the amplitude data from the fits file for each KID.

6.2.1 Spectrum contributions

When the data is passed through to KID phase, there are four noise sources contributing to the whole. Therefore, it is interesting to look at how each noise source contributes, and which noise sources are dominating. **Figure 6.5** below shows how each source contributes to the overall spectrum, using KID 35 as an example. The raw T_{sky} spectrum is plotted, plus the two KID noise sources, and the overall spectrum.

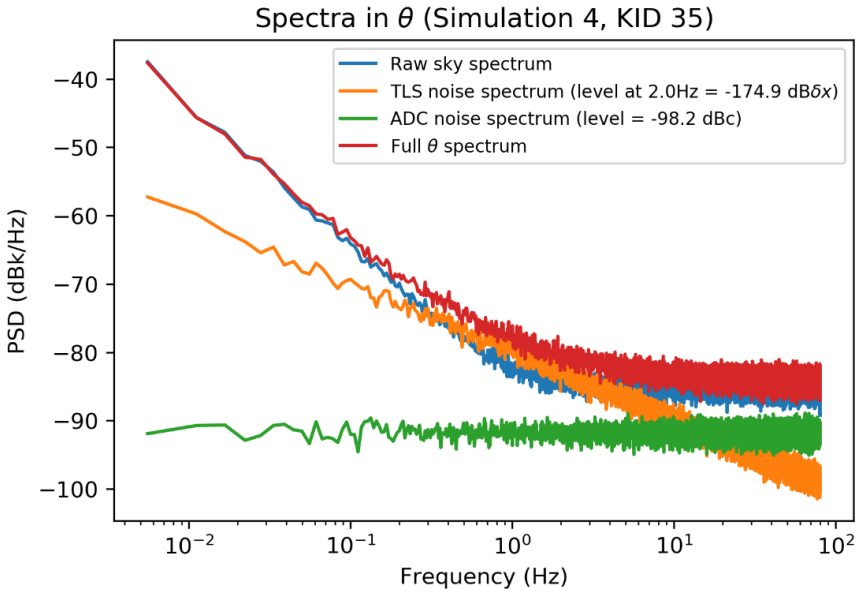

Figure 6.5: Contribution of noise sources to overall spectrum in KID phase

The plot shows how the dominant noise source changes in different frequency regimes. In the low-frequency area, the noise is dominated by the sky noise; it has a 1/f shape with a higher power than TLS at low frequencies. The TLS noise will also therefore decay slower, so there comes a point around the knee where the TLS dominates to an extent, pushing the curve up, and making the knee smoother. Finally, at the high-frequency region, both the TLS and sky noise have decayed, and the spectrum is dominated by the photon noise. The level of the ADC noise is relatively low, therefore only has a slight overall effect, but is somewhat observable at the highest frequencies in the plot.

The relative contribution of each noise source would vary to an extent between different KIDs, depending on the observation data and the Q-factors of those KIDs. Nevertheless, the plot shown above provides a reasonable depiction of how each source contributes.

6.2.2 Spectrum comparisons

The intention of simulating DESHIMA 1.0 was to then eventually replicate the observed spectra in KID phase, thereby being able to analyse the KID model. The observed phase data was obtained from fits files of the observation with run ID 1318.

In order to analyse the effectiveness in replicating the spectra, it is useful to view the observed and simulated plot simultaneously, as in the previous section. In order to try to keep the optical efficiency close to the value used, yet still attempt to observe a variety, a group of four KIDs was chosen which had optical efficiency values close to the one used. These are summarised below:

Master ID	***KID number/ID***	***Optical efficiency***
122	29	0.0193
128	35	0.0190
130	38	0.0181
131	37	0.0172

Table 6.1: Details of KIDs used for spectrum comparison plots. KIDs were chosen for the proximity to the optical efficiency value used.

The comparison spectra of the phase of these four KIDs are shown in **Figure 6.6** below, and show that the change in the RMS value of the atmospheric fluctuations has managed to change the $1/f^n$ slope such that it matches the observation data better. Although the levels of the spectra tend to vary, the general shape and the slope of the $1/f^n$ portion do tend to match well.

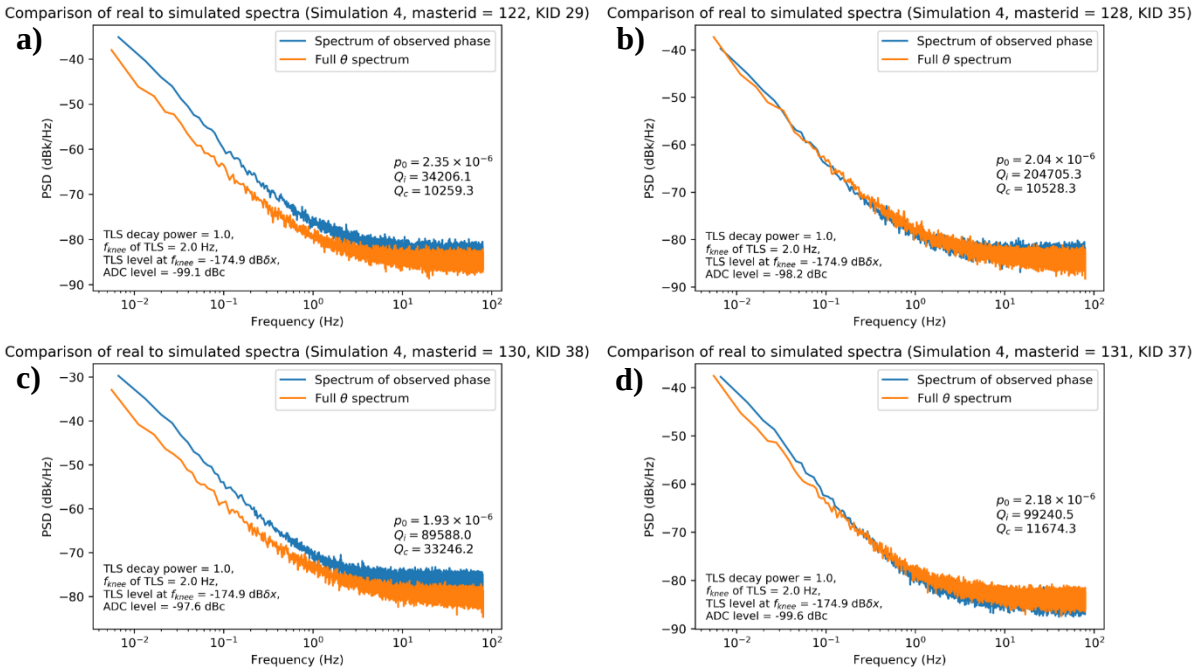

Figure 6.6: Plots of comparison of spectra in KID phase between observed and simulated data. KIDs shown **a)** 29, **b)** 35, **c)** 38, and **d)** 37. The model parameters (extracted from the fits files for each KID), along with the settings of the TLS and ADC noise levels, are displayed on each plot.

An important issue to address at this point is the offset seen in the values of the phase between measurement and simulation. The values of the phase between the real and simulated data were often large, even when the spectra appeared to match well. Therefore, in order to see whether or not the difference in the phase values was matched by a difference in noise level, **Figure 6.7** was plotted. This involved correlating the differences; the difference in phase level was plotted against difference in white noise level in dB. The difference in phase level was calculated by taking the difference of the mean of the phase values of the observed and simulated data. The difference in white noise level was calculated by taking the mean of the final 250 points of the spectra, setting to dB, and then taking the difference.

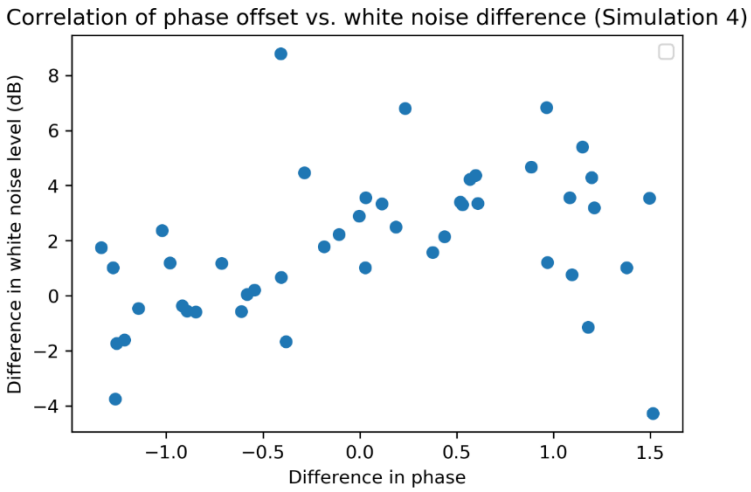

Figure 6.7: Plot showing correlation between difference in phase values, and the difference in white noise levels of the spectra (in dB)

The plot shows a slight correlation between the two, therefore the difference in the phase values does seem to have some effect on the white noise level. There also appears to be an offset; at 0 phase difference, there is a roughly 2dB difference in the white noise level, indicating a systematic effect.

The fact that there are significant differences in the values could stem from a number of causes related to the simulation and modelling of the KIDs, hence showing the limitations of the modelling. The KIDs were modelled as being symmetric, which would not have been the case in reality, as there would have been higher order effects. Furthermore, a singular value for the optical efficiency was used, whereas direct values for each channel would have provided more accuracy. The stability of the temperature in the cryostat may also not be perfect.

Additionally, the modelling necessitated certain assumptions, among them the assumption that the KIDs had been calibrated to a 300K load recently enough to the measurement to prevent significant drift off-resonance. This should have theoretically meant that all of the phase values are negative, given that the temperature was always below 300K. However, the data of the phase values showed that the phase was often positive, hence it is possible that they were not recently calibrated at 300K, or there were differences in the pipeline,

such as the method of defining the ‘zero-phase’ position. This indicates a lack of precise knowledge of the operation of the KIDs, which would likely limit the accuracy of the model.

6.2.3 Statistical analysis of differences

Given the variation clearly present in the differences between the observed and simulated data, a useful tool for analysis is to observe the statistics over all of the KIDs. This was performed by way of histograms, to see the scatter present in various elements of the difference between the observed and simulated data. Three aspects to study in comparing the real and simulated data were 1) The difference in the white noise levels, 2) The difference in the TLS noise levels, 3) The difference in the phase values. Producing histograms of these would enable a visual depiction of the scatter and any systematic effects.

The white noise level difference for the histogram was calculated in the same was as it was for the correlation plot above, i.e. taking the mean of the final 250 points, by which point the $1/f^n$ noise had died down, and the spectrum was white noise dominated. The histogram for the white noise difference is shown in **Figure 6.8**.

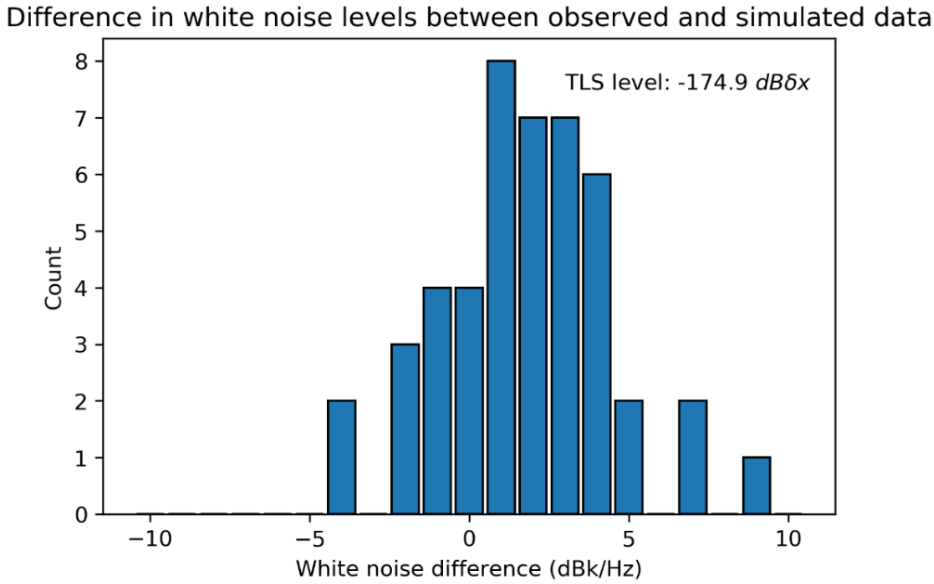

Figure 6.8: Histogram depicting difference in white noise level between real and simulated data (in dB). White noise level obtained by taking the mean of final 250 points of spectra

The TLS noise from the KID model would tend to affect the spectrum around where the knee would be. Therefore, the TLS noise difference was analysed by taking the mean of the points between 1 and 2 Hz. This histogram is shown in **Figure 6.9**.

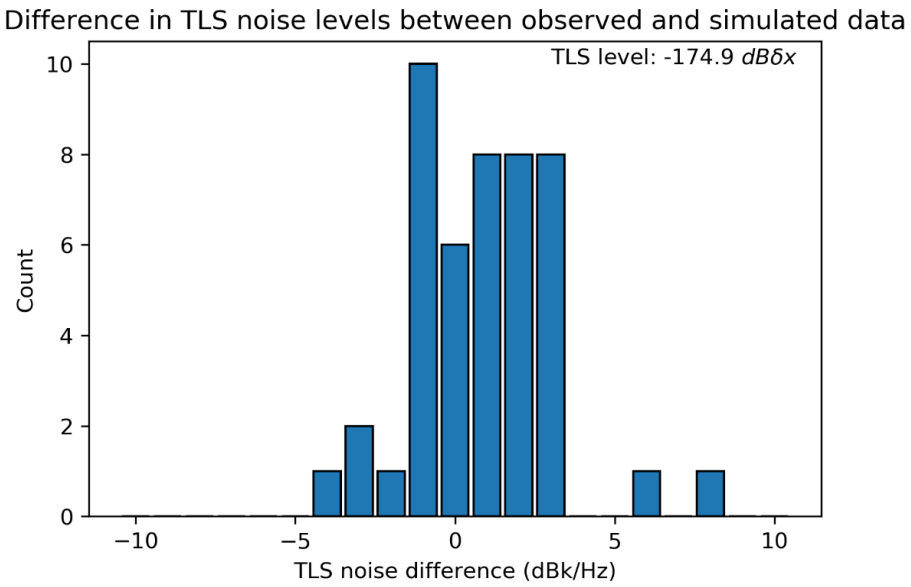

Figure 6.9: Histogram depicting difference in TLS noise level between real and simulated data (in dB). TLS noise level obtained by taking the mean of points between 1-2 Hz

The histogram of the white noise level differences shows that there is significant scatter in the levels, especially since the values shown are in decibels. It is also noticeable that there appears to be an offset from 0, given that the peak number of KIDs occurs in the bin of 0.5-1.5 dB, and the two succeeding bins are also quite populated. This indicates some systematic effect in play. The histogram of the TLS noise differences also shows a fair amount of scatter in the values, although less than what was seen with the white noise. There also does not appear to be a clear offset from 0, which is expected as the TLS noise is set based on observation data.

The scatter in both plots is possibly exacerbated by the fact that while the optical efficiency value used in the simulation was calculated only using KIDs between 350 and 370 GHz, the histograms show data for all of the KIDs. Therefore, the KIDs at the edges of the band could increase the scatter of the histograms. The spectral resolution during the simulation was also kept constant, but this should not have much effect, given that work is done in temperature rather than power.

Additionally, as mentioned earlier, the values of T_{sky} from the TiEMPO simulation were multiplied by the forward efficiency for the results seen, and in hindsight it was realised that this is likely erroneous, given that the forward efficiency is already taken into account in

the simulation. While the effect of this error is not great enough to explain the large phase differences, it would likely decrease the systematic offset seen in histogram of the white noise differences (**Figure 6.8**), and the offset in the white noise vs. phase difference plot (**Figure 6.7**). The repeat use of the forward efficiency value of 0.86 would cause an error in the gain, and so an offset in the noise levels.

The histogram of the phase differences is shown below in **Figure 6.10**. The procedure was again simply the difference in the mean phase value between the observed and simulated data. This shows a large amount of scatter compared to the ones for the noise levels. The reasons for this are not clearly known, but a likely cause is the differences in the KID model and responsivity, compared to the real KIDs, as well as possible differences in the KID calibration and operation.

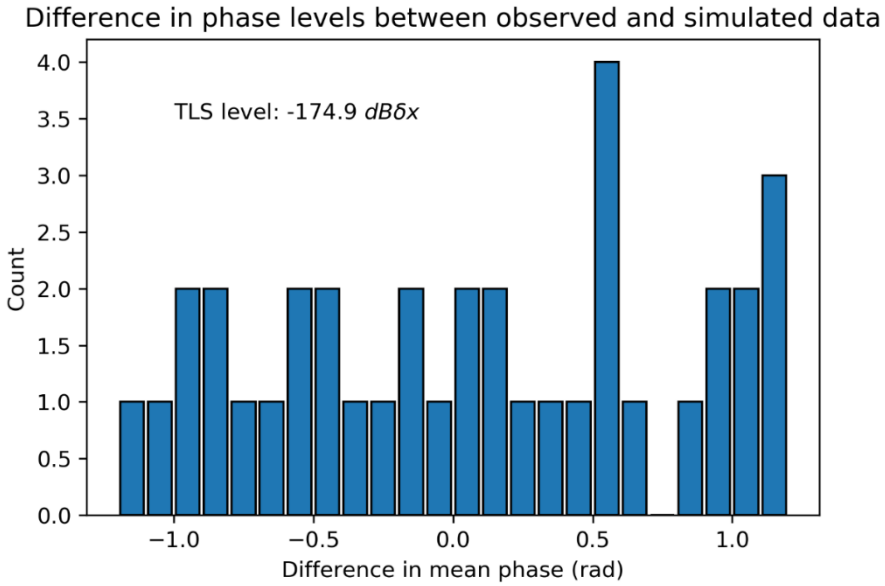

Figure 6.10: Histogram depicting difference in mean phase value between observed and simulated data

6.3 Noise integration

An important tool to study the noise sources and their effect on observations over time is using noise integration. This can show whether or not, with an increase in integration time, the noise will reduce, and what a useful integration time would be in a real observation.

6.3.1 Allan variance

The Allan variance (σ_A^2) is a commonly used device to quantify the noise integration, and hence can be used to observe the effect over integration time [14]. This is a two-sample variance, which is the variance between two time-averaged points in the time stream vs time separation. As such it simulates the effect of optical modulation such as sky chopping position on the variance of the chopped data. It is useful in analysing frequency characteristics, as it reflects the frequency dependence in spectra.

The general approach for calculating the Allan variance for a particular integration time is as follows. The time stream is divided into segments, which have the length of the integration time. An array of the mean of each segment is formed, and a difference array is formed by taking the difference between consecutive elements in the mean array. The variance of the difference array is then the Allan variance for the integration time. The integration time is then changed to display the dependence of the Allan variance on the integration time.

There is a general expected shape for an Allan variance plot, if the shape of the noise spectrum is known. **Equation (6.1)** below shows how the Allan variance is related to the integration time τ, where α is the frequency dependence of the noise spectrum, therefore the Allan variance of white noise ($\alpha = 0$) should decrease with a power of -1 with integration time [14].

$$\sigma_A^2 \propto \tau^{\alpha-1} \tag{6.1}$$

The Allan variance therefore, was calculated in the effective sky temperature domain with all of the noise sources added. The raw sky temperature data was converted to KID phase, while adding the TLS and ADC noises. This was then converted back to temperature to give the time stream in temperature with all of the noise sources. **Figure 6.11** shows an example timestream for KID 37.

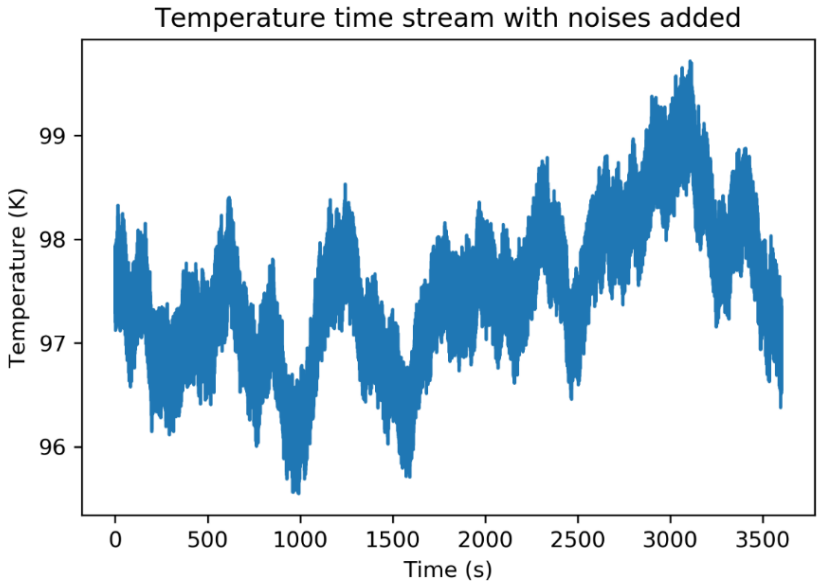

Figure 6.11: Time stream of T_{sky} from simulation, with KID noise sources added. KID 37 is depicted

Figure 6.12 below shows the resulting Allan variance plot, calculated for an on-source position, with the amount of points for integration increasing logarithmically between 10^0 and half of the total amount of points in the timestream.

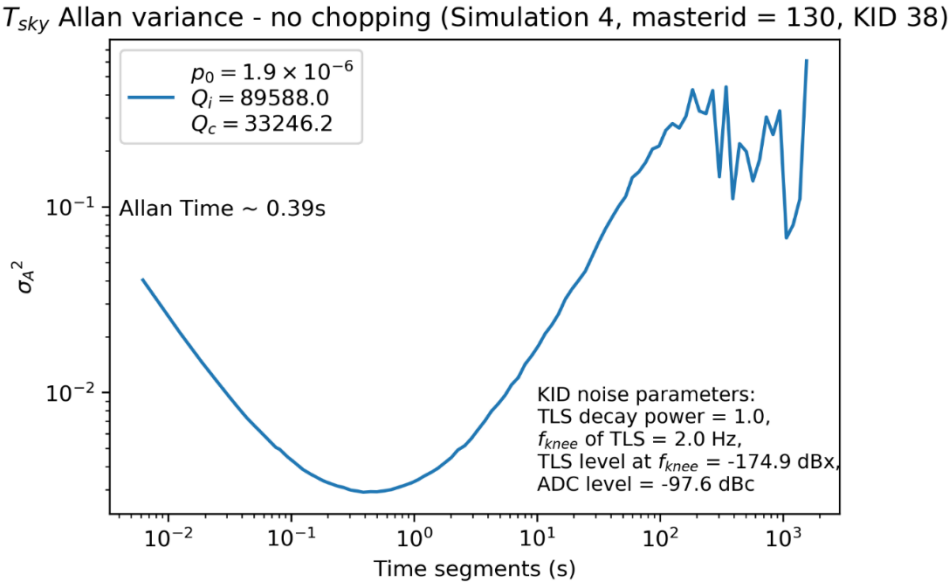

Figure 6.12: Allan variance against integration time for an on-source noise signal in temperature for KID 38. The offset has been removed for this analysis. The model parameters used are shown on the plot, along with a rough value for the Allan time (this is difficult to accurately state because of the spacing of τ values).

The plot shows that up to a certain point, the Allan variance is decreasing with integration time, but after this point the curve turns and the Allan variance starts to increase. This correlates with what is expected from **Equation (6.1)**: at low τ values, the white noise is dominating, so σ_A^2 decreases with a power of -1. After a certain point, the $1/f^n$ noise starts to

dominate, and this has a frequency dependence of $\alpha = n > 1$, therefore the Allan variance increases. Therefore, the point at which the Allan variance increases again represents a useful value, known as the Allan time. This is the maximum amount of time for which the noise can be beneficially integrated. The Allan time values tended to be around 0.5s, as expected for a spectrum with a $1/f$ knee of around 1-2 Hz

In contrast, **Figure 6.13** below shows the Allan variance plot for a noise signal that has undergone simplified chopping, i.e. the off-source signal has been subtracted from the on-source signal. The subtraction has therefore removed the sky fluctuations, and the noise sources from the KID, and left only the photon noise, which is white. It can consequently be seen that the noise is continually integrating down with a power of -1, as expected.

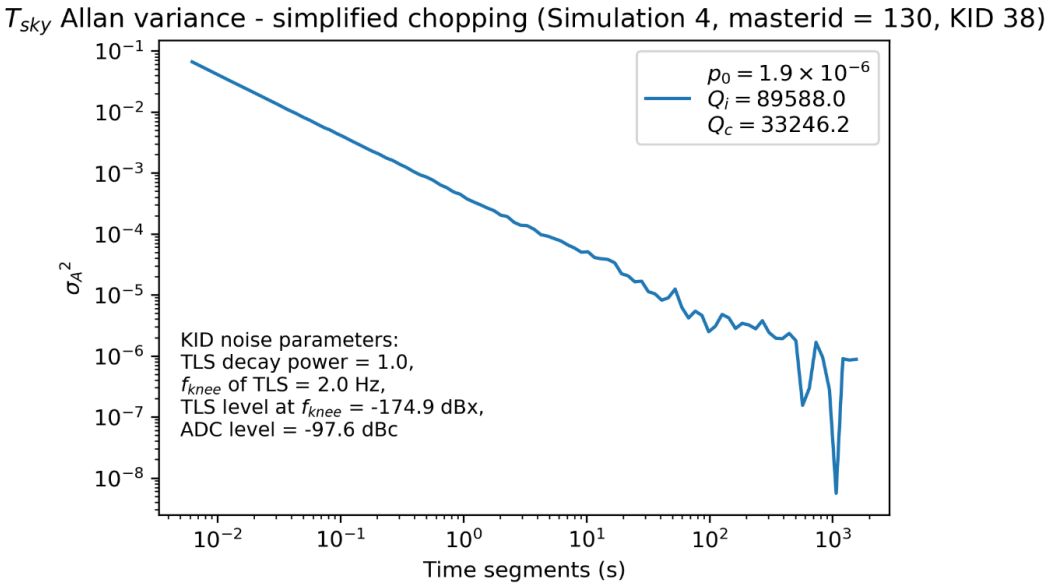

Figure 6.13: Allan variance against integration time for simplified chopping (on-source minus off). The offset has been removed for this analysis. The model parameters used are shown on the plot.

7 Conclusions

The aims of this project were, as stated in the beginning, to be able to model KIDs to convert temperature to phase whilst adding KID noise sources, replicate an observation by combining with the sky simulator TiEMPO, and to analyse the output. The success of these aims is somewhat varied. The KID model was constructed which would convert absorbed temperature to phase, after which a simulation for DESHIMA 1.0 was carried out. The combination of these two provided a replication of an observation taken by DESHIMA 1.0.

The results obtained from the replication showed some encouragement with regards to the shape of the spectra, particularly for the selected KIDs which were close to the used optical efficiency. However, the scatter in the noise level differences and the offsets and scatter in the phase values pointed towards limitations in the model, and positive values in the observed phase suggested differences in the KID calibration and operation.

The noise integration using Allan variance showed more expected results, the dependence on integration time followed a pattern which was explainable by considering the regions of white and 1/f noise domination. The Allan time values were also showing reasonable results.

It can be stated that to a certain extent the aims were completed, however some of the unexpected results obtained did indicate that there were areas in which the model could be improved. Going forward, the results obtained could be independently verified, certain changes could be made to the model to mitigate some of these unexpected results, and further additions could be made to view their effects. Possible future prospects for the model are suggested below:

- **KID asymmetry** - The KIDs are modelled as perfect symmetrical Lorentzians, which does not reflect how they behave in reality, hence the measured shape of the KIDs could replace the idealised model used.
- **Realistic chopping strategy** – In the results shown in this project, the ‘chopping’ included simply subtracting off-source from on-source. A more realistic chopping

strategy could be simulated to observe how this affects the noise and the integration thereof.

- **Improvement to TLS noise generation** – As mentioned previously, the TLS noise generation method appeared to break down for high powers. While this was tested for the range of interest and found to function without issues, this is an area where better understanding could be formed in the hope of mitigating this effect.
- **Detector/filter-specific simulation parameters** – A singular optical efficiency value was used in simulation, if the specific values for each detector could be used, this would lead to greater accuracy. Similarly, a constant spectral resolution value was used in the simulation, which could also be made KID-specific.
- **Clearer knowledge of KID calibration & operation** – If specific settings for each KID could be used (such as T_{load}), this would improve the accuracy in using the KID model. The model itself could be changed such that the measured KID circles could be used as the model. This would then no longer require the assumption of an initial phase of 0, and could account for drifts between calibration and measurement.
- **Object-oriented programming for KID model** – The current version of the KID model is a module in Python, containing various functions. Changing this to be object-oriented would simplify the code, and not require a full set of KID parameter inputs for each function.
- **Vectorised code** – In some instances, particularly when having to calculate for multiple KIDs, the code is not vectorised and makes use of for-loops. This was not a huge issue in this project, but in other instances, this could make the calculations faster.

References

[1] TU Delft, "The DESHIMA guide to the galaxy," [Online]. Available: https://www.tudelft.nl/en/eemcs/current/nodes/stories/the-deshima-guide-to-the-galaxy/. [Accessed 29 June 2020].

[2] E. Huijten, "TiEMPO: Time-Dependent End-to-End Model for Post-process Optimization of the DESHIMA Spectrometer," 2020.

[3] Y. Asaki, M. Saito, R. Kawabe, K.-i. Morita, Y. Tamura and B. Vila-Vilaro, *ALMA MEMO No. 535: Simulation Series of a Phase Calibration Schemewith Water Vapor Radiometers for the Atacama Compact Array,* 2005.

[4] T. Takekoshi, K. Karatsu, J. Suzuki, Y. Tamura, T. Oshima, A. Taniguchi, S. Asayama, T. J. L. C. Bakx, J. J. A. Baselmans, S. Bosma, J. Bueno, K. W. Chin, Y. Fujii, K. Fujita, R. Huiting, S. Ikarashi, T. Ishida, S. Ishii, R. Kawabe, T. M. Klapwijk, K. Kohno, A. Kouchi, N. Llombart, J. Maekawa, V. Murugesan, S. Nakatsubo, M. Naruse, K. Ohtawara, A. Pascual Laguna, K. Suzuki, D. J. Thoen, T. Tsukagoshi, T. Ueda, P. J. de Visser, P. P. van der Werf, S. J. C. Yates, Y. Yoshimura, O. Yurduseven and A. Endo, "DESHIMA on ASTE: On-Sky Responsivity Calibration of the Integrated Superconducting Spectrometer," *Journal of Low Temperature Physics,* pp. 231-239, 2020.

[5] P. K. Day, H. G. LeDuc, B. A. Mazin, A. Vayonakis and J. Zmuidzinas, "A broadband superconducting detector suitable for use in large arrays," *Nature,* pp. 817-821, 2003.

[6] A. Endo, K. Karatsu, Y. Tamura, T. Oshima, A. Taniguchi, T. Takekoshi, S. Asayama, T. J. L. C. Bakx, S. Bosma, J. Bueno, K. W. Chin, Y. Fujii, K. Fujita, R. Huiting, S. Ikarashi, T. Ishida, S. Ishii, R. Kawabe, T. M. Klapwijk, K. Kohno, A. Kouchi, N. Llombart, J. Maekawa, V. Murugesan, S. Nakatsubo, M. Naruse, K. Ohtawara, A. Pascual Laguna, J. Suzuki, K. Suzuki, D. J. Thoen, T. Tsukagoshi, T. Ueda, P. J. de Visser, P. P. van der Werf, S. J. C. Yates, Y. Yoshimura, O. Yurduseven and J. J. A. Baselmans, "First light demonstration of the integrated superconducting spectrometer," *Nature Astronomy,* vol. 3, p. 989–996, 2019.

[7] J. Baselmans, "Kinetic Inductance Detectors," *Journal of Low Temperature Physics,* vol. 167, p. 292–304, 2012.

[8] B. A. Mazin, *Microwave Kinetic Inductance Detectors,* 2005.

[9] M. Griffin, *Noise in Electromagnetic Radiation Detection,* Cardiff: Cardiff University School of Physics and Astronomy, 2006.

[10] J. Gao, J. Zmuidzinas, B. A. Mazin, H. G. LeDuc and P. K. Day, "Noise properties of superconducting coplanar waveguide microwave resonators," *Applied Physics Letters,* vol. 90, no. 10, 2007.

[11] J. van Rantwijk, M. Grim, D. van Loon, S. Yates, A. Baryshev and J. Baselmans, "Multiplexed Readout for 1000-Pixel Arrays of Microwave Kinetic Inductance Detectors," *IEEE TRANSACTIONS ON MICROWAVE THEORY AND TECHNIQUE,* vol. 64, no. 6, pp. 1876-1883, 2016.

[12] L. Bisigello, S. J. C. Yates, V. Murugesan, J. J. A. Baselmans and A. M. Baryshev, "Calibration scheme for large Kinetic Inductance Detector Arrays based on Readout Frequency Response," *Journal of Low Temperature Physics,* vol. 184, no. 1-2, pp. 161-166, 2016.

[13] A. Endo, K. Karatsu, A. Pascual Laguna, B. Mirzaei, R. Huiting, D. J. Thoen, V. Murugesan, S. J. Yates, J. Bueno, N. van Marrewijk, S. Bosma, O. Yurduseven, N. Llombart, J. Suzuki, M. Naruse, P. J. de Visser, P. P. van der Werf, T. M. Klapwijk and J. J. A. Baselmans, "Wideband on-chip terahertz spectrometer based on a superconducting filterbank," *Journal of Astronomical Telescopes, Instruments, and Systems*, vol. 5, no. 3, 2019.

[14] J. W. Kooi, "Advanced receivers for submillimeter and far infrared astronomy," 2008.

Appendix A Simulations log

A.1 Simulation 1

A.1.1 Simulation parameters

Simulation type: *Test*

Time simulated: *2 mins (120 s)*

Filters simulated: *All (49) (Sorted into order)*

Sampling rate: *160 Hz (19200 samples total)*

***Number of jobs in parallel**: 20*

***Simulation finished at**: 11/06/20 18:05*

A.1.2 Efficiencies

- **eta_M1_spill** – 0.99 (same as DESHIMA 2)
- **eta_M2_spill** – 0.6
- **eta_wo_spill** – 0.99 (same as DESHIMA 2)
- **eta_opt** – optical efficiency, defined as :
  eta_co*eta_lens_antenna_rad*eta_circuit*eta_IBF
- **eta_circuit –** defined as eta_filter_peak multiplied by Lorentzian shape across filters.
- **mean eta_opt between 350 and 370 GHz** - 0.0183. Use eta_opt and set other four to 1 (eta_filter_peak set to 1 for eta_ciruit).
- **eta_mb** – 0.34
- **eta_M1_ohmic, eta_M2_ohmic** – Define the same as function already in code.
- **n_wo_mirrors** = 2.

A.1.3 Weather parameters

$\boldsymbol{pwv_0} = 1.0$ mm

$\boldsymbol{El} = 60°$

A.1.4 Simulation performance

Graphical interface?: Yes

***Time taken (non-parallel):** 118.76s*

***Time taken (parallel):** 420.14s*

A.1.5 Important changes

None, test run.

A.2 Simulation 2

A.2.1 Simulation parameters

Simulation type: *Real observation replication*

Observation ID: 20171115081732 (runid = 1318)

Time simulated: *1 hour (3600 s)*

Filters simulated: *All (49) (Sorted into order)*

Sampling rate: *160 Hz (576,000 samples total)*

***Simulation finished at**: 11/06/20 22:48*

A.2.2 Efficiencies

- **eta_M1_spill** – 0.99 (same as DESHIMA 2)
- **eta_M2_spill** – 0.6
- **eta_wo_spill** – 0.99 (same as DESHIMA 2)
- **eta_opt** – optical efficiency, defined as : **eta_co*eta_lens_antenna_rad*eta_circuit*eta_IBF**
- **eta_circuit –** defined as eta_filter_peak multiplied by Lorentzian shape across filters.
- **mean eta_opt between 350 and 370 GHz -** 0.0183. Use eta_opt and set other four to 1 (eta_filter_peak set to 1 for eta_ciruit).
- **eta_mb** – 0.34
- **eta_M1_ohmic, eta_M2_ohmic** – Define the same as function already in code.
- **n_wo_mirrors =** 2.

A.2.3 Weather parameters

$\boldsymbol{pwv_0} = 1.72\text{mm}$

Windspeed = 10 m/s

$\boldsymbol{El} = 88°$

prefix_atm_data = 'aris200602.dat-'

A.2.4 Simulation performance

Graphical interface?: No

***Time taken (non-parallel):** 690.47s*

***Time taken (parallel):** 12947.69s*

A.2.5 Important changes to code

- See efficiencies. eta_opt included as additional factor when eta_chip is calculated.
- See weather parameters
- New splines created for P-Tb using filterbank.py. Note: removed progressbar and subplot animation time in filterbank.py since computer did not have this.
- Changed filter values and definition. Instead of regularly spaced filters generated between minimum and maximum frequency, array of filter frequencies used as a direct input in main.py. Frequencies obtained from DESHIMA database fits file. Filters also changed in same way in filterbank.py.
- Also made directory changes: In signal_transmitter & filterbank backslashes caused issue with Linux computer. In GiveSL.py, dots in directory, e.g. '. /K17_Table7', also removed due to problems with Linux.

A.3 Simulation 3

A.3.1 Simulation parameters

Simulation type: *Real observation replication*

Observation ID: 20171115081732 (runid = 1318)

Time simulated: *15 mins (900 s)*

Filters simulated: *All (49) (Sorted into order)*

Sampling rate: *160 Hz (576,000 samples total)*

***Simulation finished at**: 16/06/2020 14:12*

A.3.2 Efficiencies

- **eta_M1_spill** – 0.99 (same as DESHIMA 2)
- **eta_M2_spill** – 0.6
- **eta_wo_spill** – 0.86
- **eta_opt** – optical efficiency, defined as :
  eta_co*eta_lens_antenna_rad*eta_circuit*eta_IBF
- **eta_circuit –** defined as eta_filter_peak multiplied by Lorentzian shape across filters.
- **mean eta_opt between 350 and 370 GHz** - 0.0183. Use eta_opt and set other four to 1 (eta_filter_peak set to 1 for eta_ciruit).
- **eta_mb** – 0.34
- **eta_M1_ohmic, eta_M2_ohmic** – Define the same as function already in code.
- **n_wo_mirrors** = 4.

A.3.3 Weather parameters

$\boldsymbol{pwv_0} = 1.72\text{mm}$

Windspeed = 20 m/s

$El = 88°$

prefix_atm_data = 'aris200602.dat-'

A.3.4 Simulation performance

Graphical interface?: No

Time taken (non-parallel): *351.59s*

Time taken (parallel): *3254s*

A.3.5 Important changes

- Same changes still present as previous simulation, see section A.2.5.
- Change in warm optics spillover from 0.99 to 0.86 (corresponds to forward efficiency).
- Number of warm optics mirrors set to 4
- Windspeed doubled to 20 m/s

A.4 Simulation 4

A.4.1 Simulation parameters

Simulation type: *Real observation replication*

Observation ID: 20171115081732 (runid = 1318)

Time simulated: *1 hour (3600 s)*

Filters simulated: *All (49) (Sorted into order)*

Sampling rate: *160 Hz (576,000 samples total)*

Simulation finished at*: 23/06/2020 00:24*

A.4.2 Efficiencies

- **eta_M1_spill** – 0.99 (same as DESHIMA 2)
- **eta_M2_spill** – 0.6
- **eta_wo_spill** – 0.86
- **eta_opt** – optical efficiency, defined as : **eta_co*eta_lens_antenna_rad*eta_circuit*eta_IBF**
- **eta_circuit –** defined as eta_filter_peak multiplied by Lorentzian shape across filters.
- **mean eta_opt between 350 and 370 GHz** - 0.0183. Use eta_opt and set other four to 1 (eta_filter_peak set to 1 for eta_ciruit).
- **eta_mb** – 0.34
- **eta_M1_ohmic, eta_M2_ohmic** – Define the same as function already in code.

- **n_wo_mirrors** = 4.

A.4.3 Weather parameters

$\boldsymbol{pwv_0} = 1.72\text{mm}$

Windspeed = 10 m/s

$\boldsymbol{El} = 88°$

prefix_atm_data = 'aris200622.dat-'

A.4.4 Simulation performance

Graphical interface?: No

Time taken (non-parallel): *692.15s*

Time taken (parallel): *12936.76s*

A.4.5 Important changes

- Same changes still present as previous simulation, see section A.2.5.
- New ARIS data used, with RMS increased 3x to 150 μm, date code: 200622.
- Windspeed returned back to 10m/s.